

Fast and Sensitive NMR Encoding for Reversibly Bound Xenon

Im Fachbereich Physik der
Freien Universität Berlin
eingereichte

Dissertation

von

Jörg Döpfert



Berlin, im Januar 2015

Erstgutachter: Dr. Leif Schröder

Zweitgutachter: Prof. Dr. Joachim Heberle

Tag der Disputation: 6. 5. 2015

Die vorliegende Arbeit wurde in der Arbeitsgruppe von Dr. Leif Schröder am Leibniz-Institut für Molekulare Pharmakologie (FMP) in Berlin durchgeführt.

Hiermit versichere ich, die vorliegende Arbeit eigenständig und ausschließlich unter Verwendung der angegebenen Hilfsmittel angefertigt zu haben.

Berlin, den _____

Table of contents

1. Introduction	1
1.1. Molecular imaging modalities	4
1.2. Xenon biosensors	6
2. Background: NMR with hyperpolarized xenon	13
2.1. Principles of MRI	13
2.1.1. Nuclear magnetization	13
2.1.2. The inductive NMR signal	16
2.1.3. Chemical shift	17
2.1.4. Spatial encoding with gradients	18
2.1.5. Sampling k -space	20
2.1.6. Conventional pulse sequences	21
2.2. Spin hyperpolarization	25
2.3. (Hyper-)CEST detection	26
2.4. Experimental setup	31
3. Contents of this thesis	33
3.1. Optimizing Hyper-CEST imaging	34
3.1.1. Single-shot Hyper-CEST MRI	35
3.1.2. Exploiting redundancies in the spectral domain . .	38
3.1.3. Summary	42
3.2. Accelerating (Hyper-)CEST spectroscopy	44
3.2.1. Improved ultrafast CEST spectroscopy	47
3.2.2. Ultrafast Hyper-CEST spectroscopy	50
3.2.3. Ultrafast CEST imaging	54
3.2.4. Summary	56
4. Conclusion	59

Table of contents

List of publications	65
Bibliography	69
Abstract/Kurzzusammenfassung	83
A. Acknowledgments	85
B. Curriculum Vitae	87
C. Attached publications	89

Introduction

The sensitive detection of specific molecular targets is not only crucial for the visualization of biological processes within living cells or organisms (“molecular imaging”) [1], but also of great use for chemical profiling of heterogeneous mixtures or biological samples (“chemical sensing”) [2, 3]. Especially molecular imaging is a highly active field of research with great relevance for accurate and early disease detection and therapeutic monitoring. Nuclear Magnetic Resonance (NMR) may seem as an ideal candidate for these tasks, as it is a highly specific, non-invasive technique offering virtually unlimited penetration depth. It can furthermore be readily extended with imaging capabilities (magnetic resonance imaging, MRI), yielding unparalleled soft tissue contrast at sub-millimeter resolution without exposure to ionizing radiation, and therefore providing excellent clinical utility. Nevertheless, conventional ^1H MRI – that is, MRI of thermally polarized protons – is not the first choice when it comes to molecular imaging: Its relatively low sensitivity impedes the detection of relevant biochemical targets or “biomarkers” (e.g. receptors or enzymes that are overexpressed in diseased cells) *in vivo* as they are usually encountered at trace concentrations, and mainly restricts its use to the localization of highly abundant substances in biological tissues such as water and fat [4, 5].¹

Considerable efforts have been made to increase the sensitivity of conventional MRI, mostly through the use of contrast agents that alter the local magnetic environment of the detected protons (e.g. gadolinium-based complexes [7], superparamagnetic iron oxide nanoparticles [8] and chemical exchange saturation transfer [CEST] agents [9]). Even though promising, these agents have their challenges: For example, due to the low sensitivity of MRI, they often must be applied in relatively large amounts, which can lead to toxicity issues and in many cases goes along with an increased probability of altering the system under investigation due to pharmacological effects [1].

As an alternative, the use of other NMR-active nuclei such as ^{13}C , ^3He and ^{129}Xe that can be readily “hyperpolarized” [10, 11] has been proposed. Via hyperpolarization, the population difference between the nuclear spin states

¹Concentrations for molecular imaging targets are often in the range of 10^{-6} to 10^{-12} M, whereas conventional MRI is limited to detecting concentrations of 10^{-3} to 10^{-5} M [4]. For comparison, the water content in biological tissue is around 80% [6], corresponding to a concentration of around 44 M.

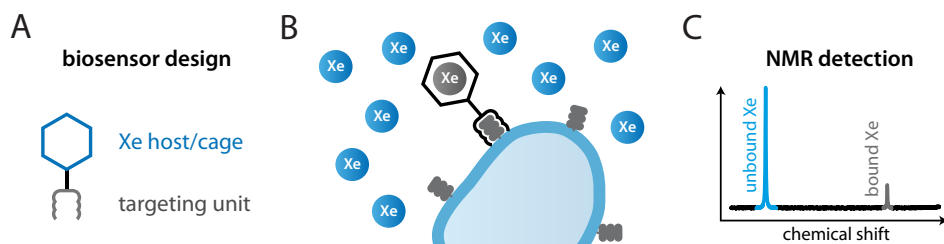


Figure 1.1.: Concept of xenon biosensors. A: Schematic biosensors design. B: Binding of a biosensor to its molecular target (e.g. a cell surface receptor). Xenon atoms act as reporters, binding to the host moiety of the biosensor. C: In a xenon NMR spectrum, xenon atoms bound to the biosensor can be easily distinguished from free unbound xenon atoms.

in an external magnetic field (e.g. “up” and “down” for spin- $\frac{1}{2}$ -nuclei) within an ensemble of spins can be increased from its rather tiny thermal equilibrium value (typically about 1 ppm) up to several percent, boosting the resulting macroscopic magnetization and hence the NMR signal by orders of magnitude. As this signal enhancement allows for the sensitive detection of rather dilute nuclear spins, the use of hyperpolarized probes for NMR and MRI holds great promise for molecular imaging and chemical sensing applications.

In this work, we use hyperpolarized ^{129}Xe (26.4% natural abundance) as an inert reporting medium. Next to other favorable properties (summarized in the box on page 7), xenon has no background signal in natural samples and can be considered biocompatible, which is reflected in a variety of *in vivo* MRI applications in both animals [12–16] and humans [17–21]. However, the inert xenon atoms alone interact rather unspecifically when introduced into the organism or the sample under investigation [22]. To report on the presence of specific molecular targets or biomarkers, so called xenon biosensors² have been developed [23]. These supramolecular constructs are typically comprised of a cage-like host moiety for binding xenon and a targeting unit (e.g. an antibody) that interacts with the structure of interest (e.g. a receptor present on the surface of pathological cells) with high specificity (see Fig. 1.1A and B). In an NMR spectrum, xenon atoms bound to the host moiety are easily distinguishable from free unbound xenon atoms, since both pools appear at markedly different NMR frequencies/chemical shifts (Fig. 1.1C). Therefore, the presence of the biosensor, and hence the presence of the target structure, can be readily detected via the NMR signal of xenon associated with the biosensor.

Since their advent in 2001 [23], various xenon biosensors have been pro-

²For the remainder of this document, the term “biosensor” or “targeted contrast agent” refers to a contrast agent compound that interacts specifically with a certain molecular target, whereas the term “contrast agent” or just “agent” may additionally refer to a compound that enhances the contrast while interacting nonspecifically.

posed for the recognition of different biochemical targets both *in vitro* and *in cellulo* [5]. In this context, the combination of hyperpolarization with chemical exchange saturation transfer, termed Hyper-CEST [24], represented a particular important step towards molecular imaging, as it allowed for the first true MRI localization of xenon biosensors in an acceptable time frame and for the detection of xenon hosts at picomolar concentrations [25, 26]. Briefly, the idea of Hyper-CEST is to transfer the recognition of the biosensors – previously achieved via the relatively small NMR signal of sensor-bound xenon – to the usually much larger signal of free unbound xenon, leading to a highly amplified detection sensitivity. Importantly, this technique relies on the fact that the binding of xenon atoms to the host moiety is reversible, i.e. temporary (which is true for many known xenon hosts). It is also worth to note that Hyper-CEST preserves spectral selectivity, such that the acquisition of Hyper-CEST spectra enables the identification of multiple different biomarkers simultaneously (“multiplexing”).

Albeit highly promising, xenon biosensors are still in their infancy, and much remains to be done to overcome existing limitations, especially when considering future *in vivo* applications. For example, the rather long acquisition times for both Hyper-CEST imaging (> 20 min per image [24]) and Hyper-CEST spectroscopy (~ 29 min per spectrum [27]) impair their practical utility. Furthermore, Hyper-CEST requires a very stable and consistent delivery of xenon to the object under investigation, which might be hard to achieve especially when examining living organisms [28].

The aim of this thesis was to tackle some of those limitations from a signal encoding perspective. To this end, we developed a toolbox of acquisition and post-processing strategies to make Hyper-CEST faster, more sensitive, and less prone to an unstable xenon delivery. We hope that our findings help to further extend the scope of xenon biosensors, in the long term ideally towards *in vivo* molecular imaging applications. It is worth to note that some of the methods developed in the course of this thesis have already been successfully applied, for example for the first *in cellulo* imaging of both targeted [29, 30] and non-targeted [P6, 31] xenon contrast agents.

This thesis is structured as follows: I continue this introductory chapter by outlining some of the most important modalities used for molecular imaging, along with their major strengths and weaknesses. Then, I put the xenon biosensor approach into context and describe it in more detail. In the second chapter, I provide the technical background knowledge to be able to follow the contents of this thesis, and introduce the setup used in most experiments of this work. The third chapter reports the main part of this work where I present the contents and key findings of this thesis in a coherent way, before I conclude in the fourth chapter. A more detailed description and discussion of many experiments of this work can be found in the journal articles related to this thesis, which are listed in the “List of publications” on page 65.

1.1. Molecular imaging modalities

Molecular imaging may be defined as the “visualization of biochemical events at the cellular and molecular level within living cells, tissues, and/or intact subjects” [1]. The detection of such events at this level requires highly sensitive techniques able to sense very low concentrations, typically in the nanomolar regime [32]. An ideal modality for molecular imaging would have the following properties:

- a high sensitivity to detect low-abundant biomarkers
- a sufficient penetration depth for the investigation of opaque samples (such as most living organisms)
- a high spatial and, where necessary, temporal resolution
- a good safety profile (in particular little or no exposure to ionizing radiation), which is especially important for repetitive studies (e.g. for monitoring treatment response)
- multiplexing capabilities, as the identification of multiple biomarkers is likely to allow for a more complete picture of a certain biological process than just a single marker, which is important for e.g. reliable diagnoses

In this section, I briefly outline some of the most important existing modalities for molecular imaging, mostly based on the excellent review article by James and Gambhir [1].

Nuclear medicine imaging techniques such as positron emission tomography (PET) and single photon emission tomography (SPECT) have traditionally been the method of choice for molecular imaging, mostly due to their high sensitivity lying in the nano- to picomolar range. They are based on radiolabeled contrast agents that are administered to the subject under investigation, where they are supposed to accumulate in areas of interest (e.g. in cancerous tissue). Subsequently, the distribution of these agents is estimated by tracing their radioactivity either with a ring detector recognizing positron-electron annihilation via two high energy (511 keV) photons (PET), or with a movable scintillation camera detecting the radiation produced during gamma decays (SPECT). While the excellent sensitivity and the virtually unlimited penetration depth of these methods result in great utility for molecular imaging, they expose the subject to ionizing radiation, have a relatively low spatial resolution (5-10 mm) and lack anatomical information as a reference (the latter issue can however be resolved by combining PET or

SPECT with magnetic resonance imaging or computed tomography). Notably, to date PET and SPECT are the only modalities that have found wide use in clinical molecular imaging applications.

On the other hand, macroscopic **optical imaging** techniques such as bioluminescence and fluorescence imaging get along without the use of harmful radiation, as they operate with agents emitting electromagnetic waves within the frequency range of the optical window. Apart from their typically very high sensitivity (pico- to femtomolar) at high spatial resolution (~ 1 mm)³ and their good ease of use (they merely require a source of light and a charge-coupled device [CCD] camera for detection, in contrast to the cyclotrons needed for PET and the superconducting magnets for MRI), optical methods provide multiplexing capabilities, as agents that emit light at different wavelengths exist. One major drawback, however, is the limited penetration depth (< 1 cm) of light photons in tissue, restricting optical imaging mainly to preclinical molecular imaging studies involving small animals.

In contrast, **computed tomography** (CT) offers practically unlimited penetration depth, since it relies on the attenuation of X-rays, which are irradiated on the sample or subject of interest at different angles. This and other advantages of CT – such as its short acquisition times, its excellent spatial resolution (< 1 mm) and its relative simplicity – have led to its widely spread clinical use for anatomical imaging. However, CT lacks soft tissue contrast and exposes the examined sample or subject to a substantial dose of ionizing radiation. Furthermore, the utility of CT regarding molecular imaging is hampered by the relatively low sensitivity of CT-compatible contrast agents.

Magnetic resonance imaging (MRI) is another tomographic technique with virtually unlimited penetration depth that allows anatomical imaging at high spatial resolution (~ 1 mm). Unlike CT, PET and SPECT, MRI is not based on ionizing radiation, but on harmless electromagnetic signals in the radio-frequency (RF) range. These are generated by the coherent precession of nuclear magnetic moments (typically from protons in water molecules) within the sample or subject to be examined, when it is placed into a strong external magnetic field.⁴ Compared to CT, MRI features excellent soft tissue contrast, and provides, in addition to anatomical information, also physiological information, e.g. about brain activity (functional MRI) or tissue water diffusion (diffusion-weighted MRI). It is therefore used for a large variety of clinical applications. However, one everlasting issue of conventional MRI is its relatively poor sensitivity (roughly in the milli- to micromolar range), hampering the detection of low abundant molecular markers as required for molecular imaging.

³Note that we are referring to macroscopic fluorescence imaging techniques suitable for *in vivo* applications here, not to fluorescence microscopy techniques (e.g. confocal microscopy).

⁴The coherence is achieved by shortly irradiating the sample with an RF excitation pulse.

In essence, although all of the above techniques have their particular strengths, and much promising work is done to overcome their limitations, per se none of them can provide all the desired features expected from an ideal molecular imaging modality. One approach to get closer to this ideal modality is the utilization of xenon contrast agents or biosensors for MRI [4], as outlined in the next section.

1.2. Xenon biosensors

The concept of xenon biosensors is one approach to combine the above mentioned advantageous properties of NMR/MRI with a high sensitivity to achieve the detection thresholds required for molecular imaging. This sensitivity gain is essentially induced by two techniques: (1) hyperpolarization of xenon to strongly increase its NMR signal per nuclear spin (see section 2.2), and (2) CEST detection to exploit the temporary nature of the binding of xenon to its host (see section 2.3).⁵

But the use of xenon as a reporting medium has further advantages (summarized in the box on page 7): For example, its large and highly polarizable electron cloud makes it highly sensitive to subtle changes in its local environment (see section 2.1.3), allowing for the detection of multiple different biomarkers at the same time (multiplexing) [34, 35], and/or for the discrimination between unbound biosensors and biosensors bound to their molecular target [23, 36].

Another favorable property of xenon is its fair solubility in liquids [38] (see Tab. 1.1). It can therefore be administered via inhalation into the lungs, where it is partly absorbed into the bloodstream and subsequently distributed

⁵The combination of both techniques is therefore called Hyper-CEST (note that to date most studies involving CEST detection are performed with conventional ¹H MRI [33]).

Table 1.1.: Xenon relaxation times (T_1) and Ostwald solubilities for different environments/phases.

	T_1	Ostwald solubility	refs.
solid phase	hours to days	–	[37, 38]
gas phase	hours	–	[39]
saline	~ 1 min ^{a,b}	0.09 ^d	[40, 41]
lipid suspensions	47 s ^{a,b}	0.62 ^b	[40]
blood	3 - 10 s ^{a,c}	0.14 ^d	[41, 42]

^a at 4.7 T ; ^b at room temperature ; ^c at 281 K ; ^d at 310 K

Why use xenon for molecular imaging?

- *MRI*: ^{129}Xe can be detected with MRI, offering unlimited penetration depth without requiring ionizing radiation. Furthermore, anatomical information is readily obtained by additionally using conventional ^1H MRI.
- *hyperpolarization*: ^{129}Xe can be readily hyperpolarized, dramatically increasing the detectable magnetization and hence enabling the recognition of low-abundant biomarkers with high sensitivity.
- *specificity*: Even though xenon is an inert noble gas, it temporarily binds to certain host molecules. These hosts can be targeted to a specific biomarker, hence comprising a xenon biosensor.
- *selectivity*: Xenon's large chemical shift range allows us to distinguish between different chemical environments, in particular between xenon associated to different biosensors (multiplexing).
- *CEST*: The reversible binding of xenon to the host molecules can be exploited with CEST, further increasing the detection sensitivity and additionally allowing for switchable contrast.
- *solubility*: Xenon is readily soluble in liquids such as water or blood.
- *biocompatibility*: Xenon is an inert gas and non-toxic at modest concentrations. When inhaled at very high concentrations (about 70%), it shows anesthetic action.
- *background signal*: Since xenon does not occur naturally in biological organism, there exists no unwanted background signal.
- *availability*: Xenon can be obtained from air, and is therefore readily available and relatively cheap (e.g. compared to ^3He).

rapidly throughout the body's tissues by circulation. As it thereby maintains its hyperpolarized state within a lifetime (T_1) of 3 - 16 seconds⁶ [42–45], xenon could be MR-detected also in organs other than the lung, such as the rodent kidney, heart [46] and brain [16, 47, 48] (MRI) as well as the human brain [49, 50] (NMR spectroscopy).

Moreover, xenon gas is largely biocompatible and benign to living organisms. When inhaled at high concentrations, it shows a (reversible) anesthetic action (minimum alveolar concentration or MAC of 71%). In fact, it has

⁶Note that T_1 of xenon in blood strongly depends on the blood oxygenation level.

several advantages over other anesthetics; its widespread clinical use is only hampered by its higher cost compared to other anesthetic substances (e.g. isoflurane) [38].

Furthermore, the detection of xenon biosensors via CEST yields not only a sensitivity boost, but also enables to switch the biosensor contrast on and off at will (by means of an RF saturation pulse, see section 2.3). This reduces the risk of false positive interpretations, as it helps to separate the effect of the contrast agent from other signal changing mechanisms, which is often an issue regarding conventional relaxivity-based MRI contrast agents [30].

Another advantageous feature of xenon biosensors is the separate administration of the targeted contrast agent (i.e. the biosensor construct) and the reporting medium (i.e. hyperpolarized xenon). This has the benefit that the biosensor molecules, after being administered, can be given as much time as necessary to accumulate in areas where the molecular targets are present and, if possible, to clear out from other areas. In a second step, hyperpolarized xenon is introduced, ideally binding quickly to the sensors, which is then finally visualized via MRI. In contrast, other hyperpolarized reporters such as ^{13}C (readily hyperpolarized with dynamic nuclear polarization, DNP), are usually part of the sensing substrate. Therefore, administration, accumulation and/or metabolism (and possibly washout) and subsequent detection of the agent have to be accomplished within the lifetime (T_1) of the hyperpolarization, which is typically around 10 - 30 s [51] – thus limiting those agents to the recognition of relatively fast biological processes. It is worth to note that the radiolabeled tracers used e.g. for PET in principle face the same issue, however, the involved radioactive isotopes have much longer life times (minutes to days) [1].

A side benefit of using MRI as detection modality is that both information on the molecular level (via xenon biosensors) as well as information on the anatomical level (via conventional ^1H MRI) can be readily obtained and accurately correlated. In contrast, PET and SPECT naturally lack anatomical information, however, both instruments can be combined with either MRI or CT to bridge this gap (“multimodality imaging” [1]).

These favorable properties have motivated the development of xenon biosensors for various applications, for example for the detection of:

- proteins such as streptavidin [23] or the major histocompatibility complex (MHC) [52]
- enzymes such as matrix metalloproteinase [53] or human carbonic anhydrase [54]
- nucleic acids [55]
- metal ions like zinc [56, 57], lead and cadmium [58]

Furthermore, after the cellular compatibility of xenon biosensors had been demonstrated [59, 60], they were employed in various *in cellulo* experiments, targeting for example:

- transferrin receptors [61]
- epidermal growth factor receptors (EGFRs, overexpressed in many cancerous cells) [27]
- CD14 cell surface proteins (primarily expressed by macrophages) [30]
- HER2 receptors (overexpressed in breast cancer cells) [35]
- human brain endothelial cells via lipopeptides [29]
- folate receptors (overexpressed in many cancerous cells) [62]

Regarding the design of xenon biosensors, the host moiety plays a crucial role: It obviously is required to have a high binding affinity for xenon, but at the same time the reversible exchange of xenon atoms in and out of the host should be relatively fast (i.e. the residence time of xenon inside the cage should be short) to allow for an efficient detection with CEST.⁷ Since xenon is a non-polar gas, various constructs with hydrophobic cavities have been proposed as xenon hosts, among them cyclodextrins [28], cucurbit- $[n]$ -urils [64, 65], and cryptophanes [66]. Of these, cryptophane-A (CrA) has become the most widely used host, not least due to its favorable binding properties (see box on page 10) for Hyper-CEST.

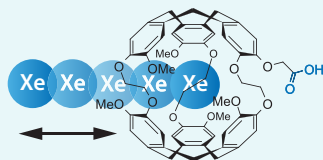
Despite their promising properties, xenon biosensors are still at an early stage of their development, and some challenges remain, especially for future *in vivo* applications. One major issue is the xenon signal: The hyperpolarization of xenon decays within seconds when dissolved in blood (see Tab. 1.1). Nevertheless, various studies report successful xenon MRI of the rodent brain upon inhalation of the noble gas [16, 44, 48, 70], indicating that the remaining signal still suffices for imaging. In addition, theoretical modeling suggested the feasibility of xenon Hyper-CEST imaging in the brain recently [35]. Moreover, as an alternative to inhalation, xenon dissolved in biocompatible lipid emulsions may be administered directly into the bloodstream

⁷However, the exchange should not be too fast either, because otherwise the two signals from the two exchanging pools (bound and unbound xenon) coalesce and cannot be distinguished anymore in an NMR spectrum [63]. Namely, the exchange rate constant should be smaller than the chemical shift difference between the two pools (often referred to as slow to intermediate exchange).

Cryptophane-A as a xenon host for Hyper-CEST

The interaction between xenon and cage-shaped cryptophane host molecules for potential biosensing applications has been well studied [34, 67]. In this context, the most commonly used construct is cryptophane-A (CrA). Its cavity size of $\sim 95 \text{ \AA}^3$ leads to an almost ideal packaging coefficient [68] (the ratio between the guest volume and the host cavity volume) with respect to xenon atoms (van-der-Waals volume $\sim 42 \text{ \AA}^3$ [5]), resulting in favorable xenon binding (binding constant $K_a = 6800 \text{ M}^{-1}$ for a slightly modified CrA cage [67]) and exchange characteristics (residence time $\tau \approx 30 \text{ ms}$ for a CrA-based biosensor [69]) regarding Hyper-CEST (both values are given in aqueous solutions at room temperature).

Experiments of this work involved, when not otherwise stated, the mono acid version of CrA (depicted below the text), where a carboxylic acid group (shown in blue) is added, allowing for the attachment of further units to functionalize the cage and/or to increase its solubility.



via injection. This method has several advantages: (1) xenon can be administered locally, (2) it possibly leads to a prolonged life time of the hyperpolarization in the range of 20 - 30 s [47, 71–73], and (3) xenon is much better soluble in lipid suspensions than in blood (see Tab. 1.1). A stronger xenon signal can furthermore be obtained by isotopic enrichment of ^{129}Xe and by optimization of the hyperpolarization process [74, 75] (another strategy for increasing the signal-to-noise ratio is to use clever signal encoding and post-processing techniques, as will be shown in section 3.1 of this thesis).

Once enough xenon signal is available to allow for MR imaging, the sensitivity of Hyper-CEST largely depends on the amount of xenon atoms that are encapsulated in the host moieties of the target-bound biosensors. A straightforward approach to increase this amount of bound xenon is to use multi-valent systems, i.e. biosensors that carry multiple xenon hosts per targeting unit. For example, multiple CrA cages have been successfully incorporated onto supramolecular scaffolds such a viral capsids [76] or bacteriophages [27, 77], allowing for sub-picomolar detection thresholds. Another approach is to utilize host moieties other than CrA that are able to accommodate multiple xenon atoms at once, such as perfluorooctyl bromide (PFOB) nanodroplets [26].

To summarize, xenon biosensor MRI is an active field of research, showing

great promise for molecular imaging. Although numerous applications and improvements have emerged in the last decade, the field is still at an early stage (e.g. yet lacking *in vivo* validation), and much research remains to be done. The next chapter will introduce the required background knowledge about MRI with hyperpolarized xenon, before my contributions to the field are presented in the main part of this thesis.

Background: NMR with hyperpolarized xenon

This chapter briefly introduces the required background knowledge to understand the contents of this thesis. Readers already familiar with the basic principles of MRI might skip the first section and instead continue reading on page 25, where I address spin hyperpolarization as a general method for NMR signal amplification. Next, I explain the concept of Hyper-CEST encoding, allowing us to detect certain xenon hosts or biosensors with strongly increased sensitivity. Finally, I describe the setup used for most of the experiments in this thesis.

2.1. Principles of MRI

A detailed description of the principles of NMR and MRI would be far beyond the scope of this thesis and numerous excellent text books and review articles covering this topic exist. However, some of the key concepts that are necessary to follow the contents of this work are briefly summarized here. For a more thorough view on magnetic resonance, the reader is referred to refs. [78–81].

2.1.1. Nuclear magnetization

Each atomic nucleus with a nonzero nuclear spin (for example, ^1H or ^{129}Xe) possesses a magnetic moment μ . Magnetic moments from single nuclei are too small to be detected through Faraday induction techniques. However, by exposing a macroscopic sample of nuclear spins (e.g. protons in a water sample) to a strong static magnetic field pointing in the z -direction, the quantized z -components μ_z of the nuclear magnetic moments eventually form a collective, measurable net magnetization \mathbf{M} along that direction. Its magnitude

$$M_0 = NP\mu_z \quad (2.1)$$

depends besides μ_z also on the number of nuclei in the sample N and the polarization P . For spin- $\frac{1}{2}$ nuclei like ^1H or ^{129}Xe , the polarization

$$P = \frac{n^\uparrow - n^\downarrow}{n^\uparrow + n^\downarrow} = \underbrace{\tanh\left(\frac{\hbar\gamma B_0}{2kT}\right)}_{\text{thermal equilibrium}} \quad (2.2)$$

relates the ensemble population difference between the spin states corresponding to parallel (\uparrow) and anti-parallel (\downarrow) orientation with respect to the static magnetic field to the total number of spins $N = n^\uparrow + n^\downarrow$ [80]. The right hand side of this expression represents the polarization in thermal equilibrium and is obtained using Boltzmann statistics,¹ revealing its dependence on the temperature T , the external magnetic field strength B_0 and the gyro-magnetic ratio γ (\hbar is the Planck constant divided by 2π , and k is the Boltzmann constant). Using $\mu_z = \frac{1}{2}\hbar\gamma$ yields

$$M_0^{\text{therm}} = \frac{N\hbar\gamma}{2} \tanh\left(\frac{\hbar\gamma B_0}{2kT}\right) \quad (2.3)$$

for the magnitude of the net magnetization in thermal equilibrium.

The time-dependent behavior of the magnetization \mathbf{M} of an ensemble of nuclear spins in the presence of a magnetic field \mathbf{B} reads [80]

$$\frac{d}{dt}\mathbf{M} = \gamma\mathbf{M} \times \mathbf{B} \quad (2.4)$$

This equation predicts that the magnetization precesses endlessly around the direction of \mathbf{B} with the so called *Larmor frequency*

$$\omega_0 = \gamma|\mathbf{B}| \quad , \quad (2.5)$$

where $|\mathbf{B}|$ is the magnitude of \mathbf{B} . However, experiments show that instead of precessing indefinitely, \mathbf{M} is driven back to its thermal equilibrium state with time. This process, which is called *relaxation*, can be phenomenologically included in Eq. 2.4 yielding the so called *Bloch equations* [82]. For a static

¹using $\frac{n^\uparrow}{n^\downarrow} = e^{\Delta E/kT}$, $\Delta E = \frac{1}{2}\gamma\hbar B_0 - (-\frac{1}{2}\gamma\hbar B_0) = \gamma\hbar B_0$ and $\tanh(x) = \frac{\exp(2x)-1}{\exp(2x)+1}$

magnetic field pointing in the z -direction, they read

$$\frac{dM_x}{dt} = \gamma(\mathbf{M} \times \mathbf{B})_x - \frac{M_x}{T_2} \quad (2.6a)$$

$$\frac{dM_y}{dt} = \gamma(\mathbf{M} \times \mathbf{B})_y - \frac{M_y}{T_2} \quad (2.6b)$$

$$\frac{dM_z}{dt} = \gamma(\mathbf{M} \times \mathbf{B})_z - \frac{M_z - M_0^{\text{therm}}}{T_1} \quad (2.6c)$$

Here, the *relaxation time constant* T_1 describes the gradual recovery of the longitudinal magnetization M_z to its equilibrium value M_0^{therm} along the direction of static magnetic field, and T_2 describes the decay of the transverse magnetization M_{\perp} due to a loss of phase coherence.²

To facilitate the solution of these equations, we introduce the complex transverse magnetization [78]

$$M_{\perp} = M_x + iM_y \quad (2.7)$$

With this, if the external magnetic field is constant, $\mathbf{B} = (0, 0, B_0)^{\top}$, one obtains the solution

$$M_{\perp}(t) = M_{\perp}(0) e^{-i\omega_0 t} e^{-\frac{t}{T_2}} \quad (2.8a)$$

$$M_z(t) = M_0^{\text{therm}} - (M_0^{\text{therm}} - M_z(0)) e^{-\frac{t}{T_1}}, \quad (2.8b)$$

showing that with time, any initial magnetization $\mathbf{M}(t=0)$ relaxes back to its thermal equilibrium $\mathbf{M}_0^{\text{therm}} = (0, 0, M_0^{\text{therm}})^{\top}$, while precessing about the z -axis with the Larmor frequency $\omega_0 = \gamma B_0$.

In conventional NMR experiments, only the transverse part of the magnetization M_{\perp} is detected. Therefore, a way to tip \mathbf{M} out of its equilibrium state $\mathbf{M}_0^{\text{therm}}$ (with $M_{\perp} = 0$) is required. This is achieved by irradiating a radio frequency (RF) electromagnetic wave on resonant with the precession frequency ω_0 of the nuclei to be tipped. If such a wave is e.g. applied along the x -axis at a magnetic field amplitude B_1 for a time t , the magnetization will be tipped about that axis by an angle of

$$\alpha = \gamma B_1 t = \omega_1 t \quad (2.9)$$

²Note that the Bloch equations are also valid when in addition to the static magnetic field with amplitude B_0 another time-dependent field $\mathbf{B}_1(t)$ is applied, as long as its amplitude B_1 is much smaller than B_0 [78].

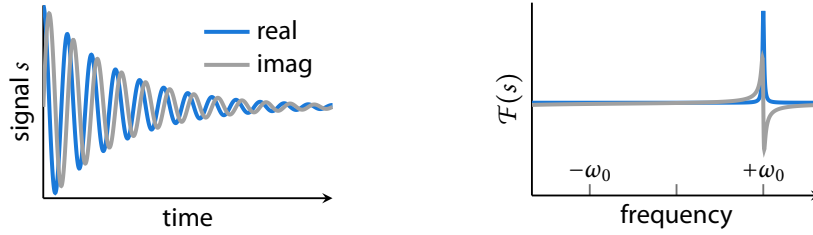


Figure 2.1.: Free induction decay signal (left) generated by precessing transverse magnetization and its spectrum as obtained via Fourier transform (right).

2.1.2. The inductive NMR signal

In a typical NMR experiment, receiver coils are placed around the sample perpendicular to the external static magnetic field (which in the following shall always point into the z -direction with strength B_0). Via Faraday induction, the precessing transverse part of the sample magnetization, M_\perp , induces an AC voltage in these coils - the NMR signal. Conventionally, two perpendicularly positioned coils are used: one to capture the “real” part or the x -component of the magnetization and one to capture the “imaginary” part or the y -component. The resulting complex signal can heuristically be seen as being proportional to M_\perp [78]. In a simple experiment with a homogeneous sample (e.g. a tube of water), where the magnetization is observed after it has been completely tipped into the transverse plane by an $\alpha = 90^\circ$ RF pulse (i.e. $\mathbf{M}(t=0) = (M_0, 0, 0)^\top$ and hence $M_\perp(t=0) = M_0$) the NMR signal is therefore given by

$$s(t) \propto M_\perp(t) \stackrel{\text{Eq. 2.8}}{=} M_0 e^{-i\omega_0 t} e^{-\frac{t}{T_2}} \quad . \quad (2.10)$$

This equation describes the so called *free induction decay* (FID), where the magnetization precesses freely in a static external magnetic field at the Larmor frequency ω_0 , decaying exponentially with T_2 . It is visualized in Fig. 2.1, left hand side.

To recover spectral information from such a time-domain signal, one can apply the Fourier transform \mathcal{F} , which in this case yields

$$S(\omega) \propto \mathcal{F}(s(t)) = \frac{M_0 T_2}{1 + (\omega - \omega_0)^2 T_2^2} + i \left(\frac{M_0 T_2^2 (\omega - \omega_0)}{1 + (\omega - \omega_0)^2 T_2^2} \right) \quad . \quad (2.11)$$

The real part of this spectrum – which is usually used for further evaluation – corresponds to a Lorentzian line shape with width $\frac{1}{\pi T_2}$ centered around ω_0 (Fig. 2.1, right). Note that it is the detection of both the real and imaginary part of the signal allows one to differentiate between positive and negative frequencies. If we had used only a single receiver coil for e.g. the real part, another peak in the spectrum at frequency $-\omega_0$ would appear.

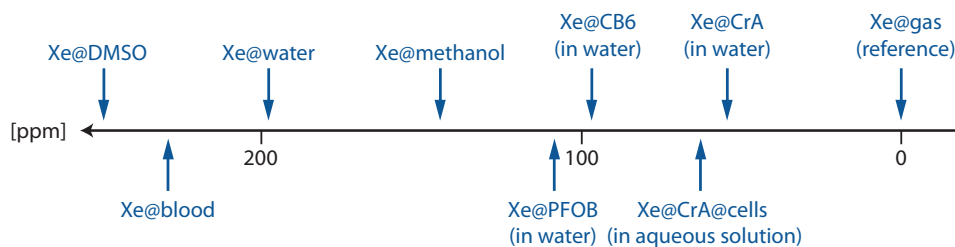


Figure 2.2.: Xenon's chemical shift range schematically depicted, adapted from [22]. Further shifts were added for xenon in cucurbit-6-uril (CB6) [65], associated to cells [P6], in perfluorooctyl bromide nanodroplets (PFOB) [31], and in methanol [83]. The exact chemical shift is of course dependent on various parameters such as temperature, pH and pressure etc. Here, rough estimates for room temperature are given.

2.1.3. Chemical shift

The retrieval of spectral information with NMR as outlined in the previous subsection would be of no use if all nuclei would precess at the same frequency ω_0 as Eq. 2.10 and 2.5 seem to predict for a static magnetic field. However, the precession frequency derived from these equations is in general dependent on the local magnetic field that the NMR-active nuclei experience. This local field in turn depends not only on the external field B_0 , but also on the chemical environment (e.g. protons in water, H_2O , as compared to protons in a methyl group, CH_3). The magnetic moment induced by surrounding electrons shields the NMR-active nuclei from the external magnetic field, leading to a local field that is slightly different than B_0 and hence yields a precession frequency ω that is also slightly different than ω_0 . The strength of the shielding depends on the density and the distribution of the surrounding electrons and therefore on the chemical environment the NMR-active nuclei are embedded in. Hence, different chemical environments will shift the frequency of the nuclei in a different way, an effect which is referred to as *chemical shift*. The chemical shift can be denoted as a frequency difference to a reference frequency $\omega - \omega_{\text{ref}}$ (e.g. $\omega_{\text{ref}} = \omega_0$) but is usually given normalized in parts per million (ppm) to make it independent from the strength of the external magnetic field:

$$\text{chemical shift} = \frac{\omega - \omega_{\text{ref}}}{\omega_{\text{ref}}} \cdot 10^6 \quad . \quad (2.12)$$

While chemical shifts between protons embedded in different molecules are usually smaller than 15 ppm [22], xenon atoms are much more sensitive to their surroundings due to xenon's large and highly polarizable electron cloud. In fact, xenon shows the largest chemical shift range among all noble gases [38] (a schematic overview of some chemical shifts of ^{129}Xe in different environments is given in Fig. 2.2). This ability to sense its environment with very high specificity is one of the properties that make xenon an ideal

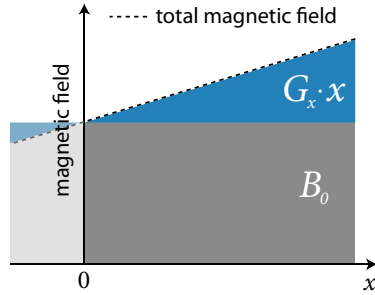


Figure 2.3: In the presence of a magnetic field gradient, the total magnetic field (calculated as a sum of the static field $|\mathbf{B}_0| = B_0$ and the gradient field $|\mathbf{B}_G| = G_x \cdot x$) and hence the Larmor frequencies become position-dependent. Typically, the strength of the static field is around a couple of Tesla [T], whereas the gradient amplitude G_x is on the order of several [mT/m].

candidate as a reporter for targeted contrast agents.

2.1.4. Spatial encoding with gradients

NMR can not only be used to get access to spectral information about the signal emitting nuclei, as illustrated in the previous sections, but also to obtain spatial information, which was first demonstrated 1973 in the groundbreaking paper of Paul Lauterbur [84]. This is achieved by spatially encoding the NMR signal with magnetic field gradients. Gradient coils produce an additional magnetic field \mathbf{B}_G along the z -direction, the strength of which varies approximately linearly along a spatial direction, e.g. along the x -axis. The total magnetic field at a certain location is then a sum of the static field \mathbf{B}_0 and this gradient field, as illustrated in Fig. 2.3.

A linear gradient is conveniently denoted as a vector

$$\mathbf{G} = \begin{pmatrix} G_x \\ G_y \\ G_z \end{pmatrix} \quad (2.13)$$

the entries of which represent the slope of the gradient in a certain direction, such that resulting magnetic gradient field is given by

$$\mathbf{B}_G(\mathbf{x}) = \begin{pmatrix} 0 \\ 0 \\ G_x x + G_y y + G_z z \end{pmatrix}, \quad (2.14)$$

where $\mathbf{x} = (x, y, z)^\top$ is the position vector. The total magnetic field then reads

$$\mathbf{B}(\mathbf{x}) = \mathbf{B}_0 + \mathbf{B}_G(\mathbf{x}) = \begin{pmatrix} 0 \\ 0 \\ B_0 + \mathbf{G} \cdot \mathbf{x} \end{pmatrix}. \quad (2.15)$$

Assume that all magnetization vectors have been tipped into the transverse plane by a 90° RF pulse, and subsequently a gradient \mathbf{G} is switched on. Due to

the spatially varying total field, the spins start to precess at different frequencies depending on their location. Using Eq. 2.5, the precession or resonance frequency at position \mathbf{x} is given by

$$\omega(\mathbf{x}) = \gamma|\mathbf{B}(\mathbf{x})| = \gamma(B_0 + \mathbf{G} \cdot \mathbf{x}) \quad , \quad (2.16)$$

where for the sake of simplicity a sample containing only a single type of nuclei has been considered (such that there are no chemical shifts). This includes that when the gradient \mathbf{G} is switched on for a certain time Δt , the precessing transverse part of the magnetization $M_\perp(\mathbf{x})$ will accumulate a position-dependent phase of

$$\varphi(\mathbf{x}) = \int_0^{\Delta t} \omega(\mathbf{x}) dt = \gamma B_0 \Delta t + \gamma(\mathbf{G} \cdot \mathbf{x}) \Delta t = \varphi_0 + \mathbf{k} \cdot \mathbf{x} \quad . \quad (2.17)$$

In the last step, the constant phase φ_0 and the spatial frequency or k -value

$$\mathbf{k} = \begin{pmatrix} k_x \\ k_y \\ k_z \end{pmatrix} = \gamma \Delta t \mathbf{G} \quad (2.18)$$

were defined. After switching off the gradient field, the nuclear spins in the sample precess at their original frequency $\omega_0 = \gamma B_0$ again and the NMR signal is recorded. To calculate this signal that is now induced in the receiver coil, we have to integrate Eq. 2.10 over the sample's volume:

$$S(t) \propto \int |M_\perp(\mathbf{x})| e^{-i(\omega_0 t + \varphi(\mathbf{x}))} e^{-\frac{t}{T_2(\mathbf{x})}} d\mathbf{x} \quad . \quad (2.19)$$

Neglecting relaxation effects ($T_2 = \infty$) for simplification and assuming that all the initial longitudinal magnetization $M_0(\mathbf{x})$ has been tipped into the transverse plane by the 90° pulse ($M_\perp = M_0$), this expression can be rewritten as

$$\begin{aligned} S(\mathbf{k}, t) &\propto \int M_0(\mathbf{x}) e^{-i(\omega_0 t + \varphi_0 + \mathbf{k} \cdot \mathbf{x})} d\mathbf{x} \\ &= e^{-i(\omega_0 t + \varphi_0)} \int M_0(\mathbf{x}) e^{-i\mathbf{k} \cdot \mathbf{x}} d\mathbf{x} \quad , \end{aligned} \quad (2.20)$$

which means that the signal magnitude is proportional to the Fourier transform of the initial longitudinal magnetization $M_0(\mathbf{x})$, i.e. the spatial distribution of the initial magnetization. If the signal $S(\mathbf{k})$ is recorded for a sufficiently high number of different k -values, then such a “magnetization image” (in the simplest case reflecting a density map of the NMR-active nuclei under investigation) can be obtained by a simple inverse Fourier transform:

$$M_0(\mathbf{x}) \propto \int S(\mathbf{k}) e^{i\mathbf{k} \cdot \mathbf{x}} d\mathbf{k} \quad . \quad (2.21)$$

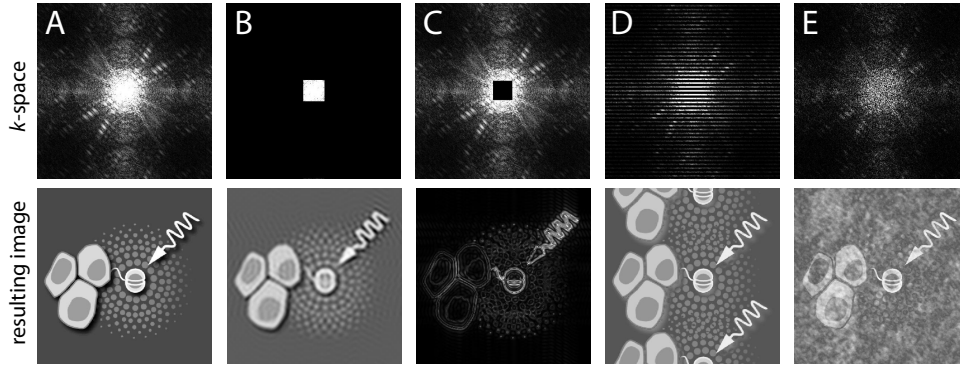


Figure 2.4.: Effects of k -space sampling on the resulting image. A: Fully Nyquist-sampled k -space (top) from the original image (bottom). B: Omitting the high frequencies in k -space and thus only retaining the center yields a loss in resolution. However, image contrast is preserved. C: On the other hand, a contour image which contains the details but hardly any contrast is obtained when only the high frequencies are sampled. D: Leaving out every second line in k -space leads to folding of half-copies into the original image since the Nyquist criterion (Eq. 2.22) is violated. E: Sampling random k -space points (again half of the data is sampled, as in D) leads to incoherent, noise-like folding artifacts.

The different magnitudes of \mathbf{k} are achieved by changing the gradient strength and/or the duration it is switched on before the signal is recorded (see Eq. 2.18). How densely the signal has to be sampled in k -space or Fourier space to obtain an artifact-free image is briefly discussed in the next section.

2.1.5. Sampling k -space

One might ask the question of how many and which data points have to be sampled in k -space for an efficient spatial NMR encoding. Briefly speaking, this can be answered as follows:

1. The spatial extent of the sample dictates the minimum spacing between two neighboring k -space points via the Nyquist sampling criterion.
2. The desired spatial resolution of the image in a given spatial direction can be adjusted by varying the maximum k -value in this direction.

The first statement is derived by considering the sampling process as a convolution of the “true” NMR signal with a comb function, and Fourier transforming the result into image space taking into account the Fourier convolution theorem. Here, just the results are given, stating that the k -space step size in one direction Δk must be smaller than 2π divided by the sample’s extent A in that direction (Nyquist criterion):

$$\Delta k \leq \frac{2\pi}{A} \Leftrightarrow A \leq \frac{2\pi}{\Delta k} = L \quad . \quad (2.22)$$

In the last step, the field of view (FOV) L was introduced. Typically, the k -values are sampled equidistantly, and hence the sampling pattern along one direction is given by

$$-k_{\max}, -k_{\max} + \Delta k, -k_{\max} + 2\Delta k, \dots, 0, \Delta k, 2\Delta k, \dots, k_{\max} - \Delta k, \quad (2.23)$$

where k_{\max} is the maximum k -value or the magnitude of the highest spatial frequency.

The second point can be understood by considering that a high spatial resolution enables to reveal small details in an object. As the spatial image originates from a Fourier transform, that is, a superposition of wave functions with different spatial frequencies, it is obvious that only wave functions with small wave lengths – i.e. high frequencies/ k -values – are able to resolve such small details. Upon closer investigation, one can derive the following expression for the spatial resolution in a given direction:

$$\Delta x = \frac{\pi}{k_{\max}} = \frac{\text{FOV}}{\text{number of sampling points}}. \quad (2.24)$$

The rightmost expression was derived by considering that k_{\max} equals half the number of sampling points multiplied by Δk and then using Eq. 2.22.

Some examples illustrating the effects of low and high frequencies in k -space and sub-Nyquist-sampling are depicted in Fig. 2.4.

2.1.6. Conventional pulse sequences

As discussed above, MRI data is acquired in Fourier- or k -space. The different k -values are achieved by applying magnetic field gradients with varying strengths and/or durations in different directions. The previous section indicated which k -values need to be acquired to obtain artifact-free images at the desired resolution. However, no remarks were made about how exactly these values should be acquired. In fact, there exist numerous acquisition strategies consisting of sequences of RF and gradient pulses, commonly referred to as *pulse sequences*. In the following, some standard pulse sequences that were used in this work are briefly described.

Gradient-echo based sequences

Gradient-echo based sequences are probably the most frequently used MRI sequences, not least due to their simplicity. A **simple gradient-echo (GRE)** sequence in two dimensions is depicted on the left side of Fig. 2.5A. Initially, a frequency-selective excitation RF pulse with an angle α (usually smaller or equal to 90°) is applied to tip the spins into the transverse plane. The gradient in z -direction that is active during the RF pulse (called a *slice-selection* gradient) ensures that only the spins in a thin plane perpendicular to that direction

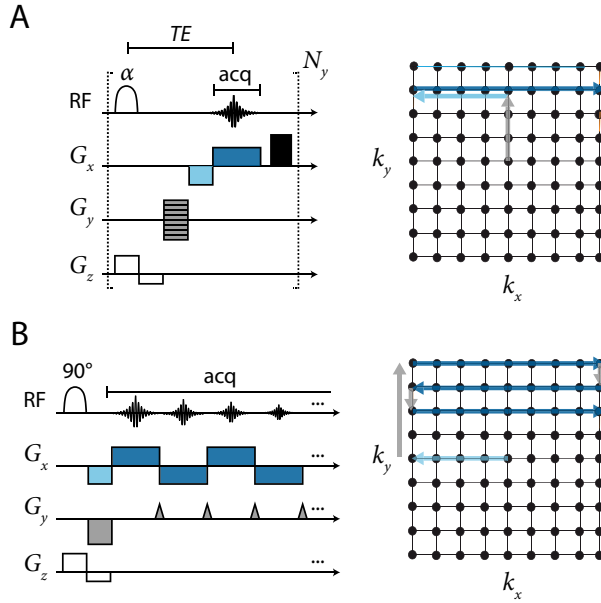


Figure 2.5: Sequence diagram and k -space trajectory of two gradient-echo (GRE) based sequences. A: Conventional gradient-echo imaging sequence. The RF-axis shows the shaped excitation pulse with an tip angle of α and the acquired NMR signal. In the gradient axis, white boxes stand for slice-selection, gray for phase-encoding, light blue for read-dephase, dark blue for readout and black for spoiler gradients. B: Echo planar imaging (EPI) sequence for a fast k -space acquisition.

are excited, leaving the remaining spins untouched since they do not fulfill the resonance condition. Hence, only a slice of the entire sample contributes to the NMR signal, reducing the imaging problem from 3D to 2D.

Directly after excitation, another gradient in z -direction is applied, but this time with the opposite sign. This refocusing gradient undoes the defocusing effects that occurred during the excitation. At this point, we have a slice of excited spins which precess at the same frequency without phase difference. Hence we are in the center of k -space, $\mathbf{k} = (k_x, k_y)^\top = (0, 0)^\top$. Next, a so called *phase-encoding* gradient is applied along the k_y -direction. This “moves” the current k -space position along the y -axis (2.5A right, gray arrow) to a certain value, i.e. $\mathbf{k} = (0, k'_y)^\top$. Then, the *read-dephase* gradient (light blue) sets the position in k_x -direction to the outermost value, i.e. $\mathbf{k} = (-k_{x,\max}, k'_y)^\top$. Subsequently, the *read* gradient (dark blue) is switched on for a certain time, moving the k -space position gradually along the k_x -axis to $\mathbf{k} = (k_{x,\max}, k'_y)^\top$ while simultaneously the NMR signal is sampled in equidistant intervals (Eq. 2.23, remember that the k -value depends also on the time that the gradient is switched on, Eq. 2.18). This way, an entire line in k -space is recorded. After all remaining transverse magnetization has been destroyed by a *spoiler-gradient* (black), the whole process is repeated N_y times with different strengths of the phase-encoding gradient, such that in the end all necessary k -space lines are sampled. During the readout step, the spins packets occur in k -space with conditions ranging from initially maximally dephased ($k_x = -k_{x,\max}$) over maximally rephased ($k_x = 0$) to maximally dephased again (this time in the opposite direction, $k_x = k_{x,\max}$). Since the NMR signal is maximized if all spins in the sample precess in phase and reduces as their phase difference grows, the recorded signal increases until $k_x = 0$ (after

the first half of the total duration of the readout) and then decreases again (see 2.5A left, signal curve above the read gradient). Such a signal form is called a *gradient-echo*, since gradients are used to defocus and then refocus the spins. The time TE between RF excitation and formation of the gradient-echo is called *echo time*. After acquisition of the entire k -space, a spatial image is readily obtained by a 2D Fourier transform.

Another gradient-echo based sequence, which is designed for fast acquisition, is the **echo planar imaging (EPI)** sequence. Here, multiple gradient-echoes are acquired after only one excitation pulse. The sequence diagram is shown in Fig. 2.5B, left. After excitation and slice-selection, the k -space position is set to $\mathbf{k} = (-k_{x,\max}, -k_{y,\max})$ and a single line is recorded as previously. Then, a short phase-encoding gradient (also called *blip*) moves the k -space position to the following line, which is subsequently recorded by switching on the read gradient in the opposite direction (moving k_x now from $k_{x,\max}$ to $-k_{x,\max}$). This is repeated until the full k -space is acquired. Since an entire image can be encoded with a single RF excitation pulse (*single shot*), the acquisition time can be reduced to a minimum. However, gradient imperfections and the relaxation based signal decrease during recording (indicated by decreasing gradient echo amplitudes in the figure) can cause artifacts in the final image and make EPI less robust than conventional gradient-echo imaging.

Spin-echo based sequences

When longitudinal magnetization is excited into the transverse plane, Eq. 2.6 and Eq. 2.8 predict that the transverse part of it will start to precess and gradually decrease with T_2 . This relaxation process is driven from randomly fluctuating local magnetic fields, which originate from Brownian motion and

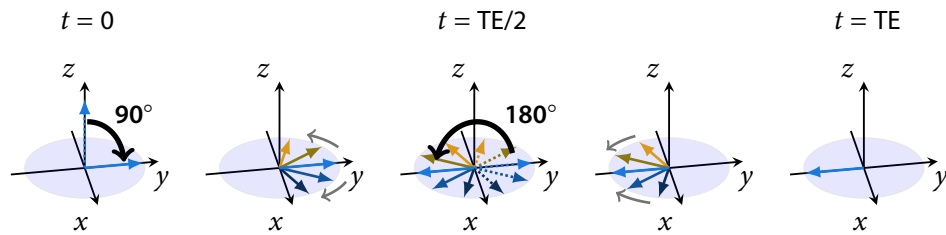


Figure 2.6.: Formation of a spin-echo, explained in the rotated frame of reference, neglecting T_2 relaxation decay for the sake of simplicity. The 90° pulse at $t = 0$ flips the longitudinal magnetization into the transverse plane. Then, the transverse magnetizations from different spin packets experiencing different magnetic fields due to inhomogeneities precess at different speeds. Some rotate faster (dark blue) and some slower (orange) than the ideal Larmor frequency. The application of the 180° pulse at $t = TE/2$ reverses the situation: Now the slower spin packets are in front of the faster ones, so that they start to rephase. At $t = TE$, the fast spins caught up the slow ones, and for this moment, all spins are in phase again: A spin-echo has formed.

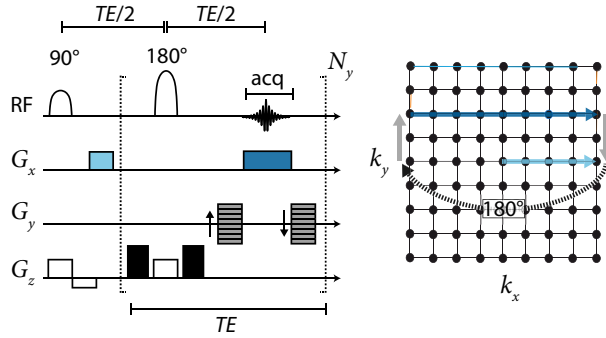


Figure 2.7: Sequence diagram and k -space trajectory of a turbo spin echo (TSE) sequence. The effect of the 180° refocusing pulse is displayed as a dashed arrow in the k -space trajectory.

molecular tumbling of nearby magnetic moments (e.g. nuclei or electrons) and other incoherent mechanisms. In general however, one will observe a faster decay of transverse magnetization with T_2^* and not with the predicted intrinsic T_2 ($T_2^* \leq T_2$). The reason lies principally in local magnetic field inhomogeneities (e.g. coming from inhomogeneities of the external static magnetic field or from susceptibility differences within the sample), which lead to an additional dephasing between spins. A *spin-echo* is another type of echo, which forms when spins packets that were dephased due to such static magnetic field inhomogeneities get rephased. It is generated by applying a 180° refocusing RF pulse after the 90° excitation pulse, as illustrated in Fig. 2.6. Spin-echoes can be useful in various situations, for example when T_2 is rather long and a T_2^* is rather short. Then, the fast decay of magnetization with T_2^* can be circumvented by acquiring spin-echoes, which decay with T_2 .

By including imaging gradients, spin-echoes can also readily be used for image formation. A variant for fast imaging, the so called **turbo spin echo (TSE)** sequence (also called RARE, rapid acquisition with relaxation enhancement), is depicted in Fig. 2.7. Here, multiple spin-echoes are formed in a single shot, that is, after a single excitation pulse. First, a slice is excited by a 90° RF pulse, and then the read-dephase gradient moves us to $\mathbf{k} = (k_{x,\max}, 0)^\top$. Next, the 180° refocusing pulse changes the sign along k_x , such that $\mathbf{k} = (-k_{x,\max}, 0)^\top$. It is surrounded by spoiler-gradients that destroy any unwanted magnetization from outside the selected slice. Next, the phase-gradient moves us to the desired k_y -position, $\mathbf{k} = (-k_{x,\max}, k'_y)^\top$. Subsequently, both the receiver and the read-gradient are switched on, and the entire k -space line is acquired. Note that after half of the acquisition time, spin-echo and gradient-echo coincide. After acquisition on the entire line, the phase-encoding gradient is switched on in the opposing direction to achieve $k_y = 0$. From this point, the 180° pulse – readout combination is repeated multiple times for different phase-encoding gradient strengths, such that in the end the whole k -space is covered. The TSE sequence is a noteworthy single-shot alternative to EPI, since it may yield more signal-to-noise if T_2 is sufficiently long, and it is less prone to artifacts.

2.2. Spin hyperpolarization

One major limitation for the use of proton NMR in molecular imaging is its relatively low sensitivity. This can be seen when evaluating the thermal proton spin polarization (Eq. 2.2) at body temperature ($T = 37^\circ \text{C}$) in a rather strong external field of 9.4 T, resulting in $P = 0.003\%$. This indicates that only a very small fraction of the total amount of spins contributes to the NMR signal, making it difficult to detect low-abundant molecular markers.

One possibility to increase the polarization is to reduce the temperature and to increase the static magnetic field. However, to make most of the spins contribute to the signal, one would need to go down to the milli-Kelvin range, even at strong magnetic fields – rendering this approach impractical for *in vivo* applications. Nevertheless, high polarization values can be obtained for some nuclei also at room temperature by a process called *hyperpolarization*. Here, the spin system is artificially driven out of its thermal equilibrium (Fig. 2.8A) to strongly increase the resulting magnetization and hence the signal. ^{129}Xe can be very efficiently hyperpolarized by *spin-exchange optical pumping* (SEOP) [85, 86], which is conceptually depicted in Fig. 2.8B. First, a droplet of an alkali metal (most often rubidium) is positioned in a weak magnetic field and heated up. Its vapor is illuminated by circularly polarized laser light aligned with the magnetic field and tuned to the D_1 transition (794.7 nm for rubidium) to spin-polarize the electrons (optical pumping). These can then transfer their polarization onto the nuclear spin of the xenon atoms by Fermi-contact hyperfine interactions via binary collisions (dominant at multi-atmosphere pressures) and via forming van-der-Waals complexes (dominant at lower pressures).

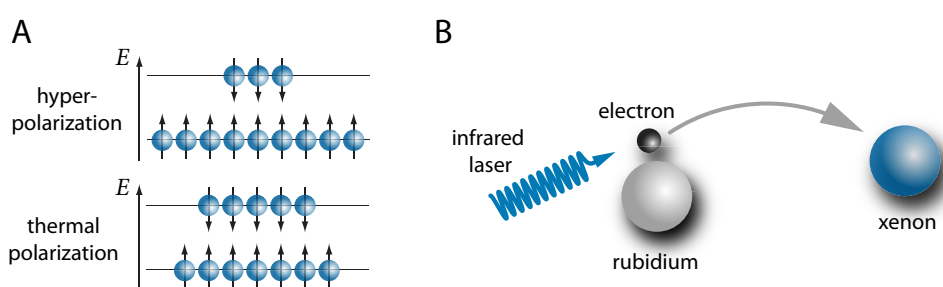


Figure 2.8.: A: Concept of hyperpolarization (adapted from ref. [5]). In thermal equilibrium at room temperature (bottom), the population density of nuclear spins aligned parallel to the external magnetic field (low energy state) is only marginally larger than the population density of spins aligned anti-parallel (high energy state). Hyperpolarization means over-populating one energy level far beyond the thermal equilibrium (top), thereby increasing the resulting macroscopic magnetization. B: Concept of spin-exchange optical pumping (adapted from ref. [10]). An infrared laser polarizes the electrons of rubidium atoms exposed to a weak magnetic field, which then transfer their polarization to xenon nuclei via hyperfine coupling.

In literature, signal enhancements of multiple orders of magnitude were reported for hyperpolarized xenon [28, 85]. The polarizer built in our lab in Berlin currently achieves a xenon polarization as high as 25% in continuous flow mode [87], corresponding to an amplification factor of nearly 30 000 compared to thermally polarized nuclei. Other polarizers can achieve even higher polarizations of around 65% [74] in continuous flow.

2.2.1. NMR detection of hyperpolarized magnetization

As described in the previous sections, the initial (hyperpolarized or thermally polarized) magnetization, that is aligned along the axis of the static magnetic field, has to be tipped into the transverse plane by an RF excitation pulse in order to be detectable with NMR or MRI. Conventional MRI pulse sequence design typically relies on the fact that this initial magnetization eventually recovers to its thermal equilibrium $M_0 = M_0^{\text{therm}}$ due to T_1 relaxation (see Eq. 2.8), such that subsequently further RF pulsing can be employed. On the other hand, when dealing with hyperpolarized nuclei, the initial hyperpolarized state $M_0 = M_0^{\text{hyp}}$ will not be recovered by relaxation, but the magnetization will instead decay to its thermal equilibrium value, which is negligible compared to the hyperpolarized value $M_0^{\text{therm}} \ll M_0^{\text{hyp}}$. Briefly speaking, the magnetization of hyperpolarized nuclei is non-renewable [88]. This has some implications on the signal detection strategies: For conventional MRI with thermally polarized nuclei, gradient-echo sequences are most often used. Here, after a low flip angle excitation and the acquisition of one line in k -space, the magnetization relaxes back to its steady state quickly and subsequently the next line can be acquired and so on. For hyperpolarized nuclei, if gradient-echo sequences are used, each excitation uses up a certain fraction of the hyperpolarized magnetization such that only a certain amount of k -space lines can be acquired before the hyperpolarization is lost. Furthermore, the gradient-echo sequence should be combined with a variable excitation flip angle to ensure the same amount of initial magnetization for each k -space line [89]. Alternatively, sequences such as EPI or TSE can be employed to use the whole initial hyperpolarized magnetization efficiently for the acquisition of an entire image in a single-shot. As will be described in section 3.1.1, we found these single-shot sequences to be particularly useful for our CEST MRI experiments.

2.3. (Hyper-)CEST detection

As depicted in Fig. 1.1A, xenon based contrast agents for molecular targets usually consist of a targeting unit and a xenon binding site (e.g. a molecular cage with hydrophobic cavity, such as Cryptophane-A, see box on page 10). Due to their large electron cloud, the xenon atoms sense whether they

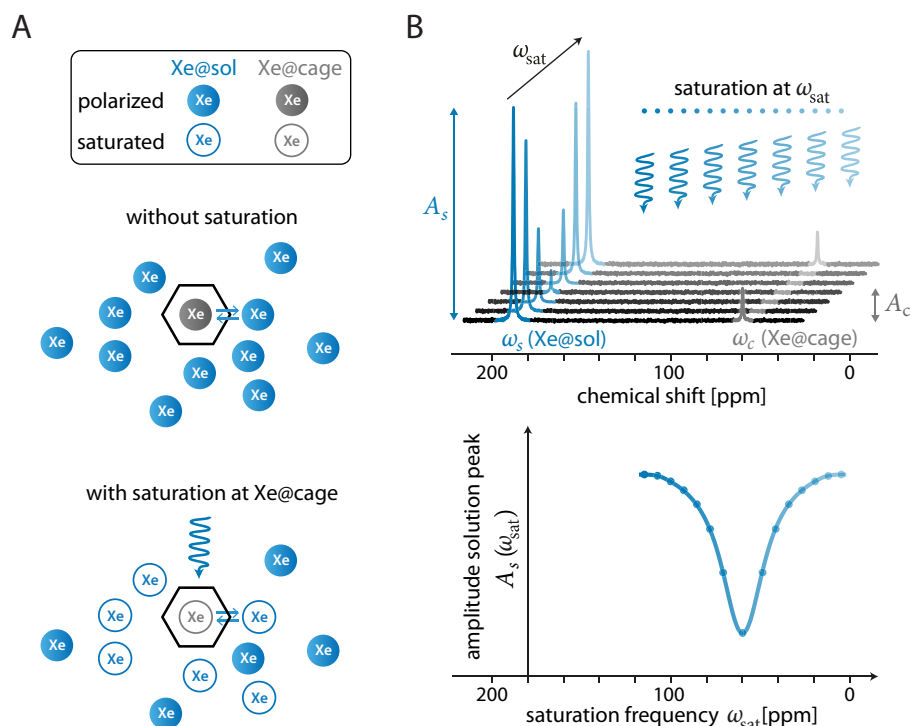


Figure 2.9.: Principle of Hyper-CEST detection. A: Without saturation, all xenon atoms remain hyperpolarized. When a saturation pulse is applied at the frequency of Xe@cage , ω_c , the nuclei inside the cage get depolarized. Due to chemical exchange, these depolarized atoms accumulate in the solution pool Xe@sol . B: Schematic of an exemplary direct NMR spectrum of xenon dissolved in an aqueous solvent containing Cryptophane-A as molecular cage (top) and corresponding Hyper-CEST spectrum (bottom). The large blue peak in the direct spectrum stems from free xenon in solution, and the small gray peak from xenon inside the cage. The chemical shift reference (zero on the horizontal axis) is the frequency of xenon in the gaseous phase (peak not shown). As the saturation pulse frequency (blue arrows) approaches the Xe@cage resonance, the amplitude of the Xe@sol peak A_s gradually decreases due to saturation transfer. This results in a negative peak at ω_c in the corresponding Hyper-CEST spectrum $A_s(\omega_{\text{sat}})$.

are unbound in solution (Xe@sol) or entrapped in such a molecular cage (Xe@cage); see Fig. 2.9A, top. This is reflected in a large chemical shift difference between the two signals in an conventional direct NMR spectrum (Fig 2.9B, top, first spectrum), that allows us in principle to detect the presence of the contrast agent via the Xe@cage resonance. Molecular imaging however aims for the detection of very low agent concentrations in the nano- to picomolar range and hence the peak amplitude of caged xenon A_c is in general much smaller than the amplitude of xenon in solution A_s . Despite the amplification through hyperpolarization, the Xe@cage peak is often even hidden below the noise level, so that the direct detection of entrapped xenon requires extensive signal averaging and long acquisition times, especially for imaging applications [90]. An alternative detection technique applying chemical

exchange saturation transfer (CEST) [33] to hyperpolarized nuclei (Hyper-CEST) was developed in 2006 in the lab of Alexander Pines [24], using the abundant pool of Xe@sol with amplitude A_s for detection instead of the dilute pool of Xe@cage. This indirect approach exploits the fact that the binding of xenon to the host structure is reversible, i.e. the xenon atoms continuously exchange in and out of the cage (Fig. 2.9A).

The idea of Hyper-CEST is as follows. Prior to acquiring the signal of Xe@sol and determining its amplitude A_s , a saturation pulse is applied on resonant with entrapped xenon (Xe@cage), i.e. $\omega_{\text{sat}} = \omega_c$, see Fig. 2.9A, bottom. This pulse depolarizes the Xe@cage atoms, which after a short time exchange into solution and are then replaced by fresh, hyperpolarized xenon atoms from the Xe@sol pool. As this process repeats rapidly while the saturation pulse is switched on, the depolarized atoms accumulate in solution and hence the magnetization of the Xe@sol pool shrinks (fourth spectrum in Fig. 2.9B, top). Hyper-CEST contrast agents are hence made visible via a switchable signal loss. Since every cage molecule typically depletes the polarization of many hundreds of xenon atoms (the exact number depends on the residence time of xenon inside the host and the saturation pulse length), Hyper-CEST greatly enhances the detection threshold and allows for the measurement of much lower agent concentrations compared to direct NMR detection. The mentioned signal loss can be quantified by subtracting the signal of Xe@sol acquired with on-resonant saturation as explained above, from a reference signal of Xe@sol with either no saturation pulse (Fig. 2.9A top), or with a sufficiently far off-resonant saturation pulse.

Hyper-CEST can not only reveal the presence of a certain contrast agent, but also allows for the retrieval of spectral information, which can be e.g. used to detect multiple agents resonating at different frequencies. To obtain such CEST spectra, the saturation pulse frequency ω_{sat} is varied and the amplitude of the solution peak A_s is extracted for each ω_{sat} and then plotted against ω_{sat} (Fig. 2.9B, bottom). Since CEST involves signal depletion, each peak in the direct spectrum yields an inverted peak in the CEST spectrum. Maximum depletion is achieved when the saturation pulse irradiates on-resonant with Xe@cage ($\omega_{\text{sat}} = \omega_c$) and hence the CEST spectrum has a minimum at this frequency. The further off-resonant the saturation pulse frequency is tuned, the less effective the saturation mechanisms works and hence the weaker is the signal loss.

Hyper-CEST can also be easily combined with MR imaging. To this end, instead of determining the amplitude of the Xe@sol peak as described above, we use the Xe@sol signal after the saturation preparation to generate an MR image with e.g. one of the imaging sequences presented in section 2.1.6. Similar to the case of CEST spectroscopy as seen in Fig. 2.9, varying the saturation frequency prior to acquiring the MR images leads to maximum signal depletion when we irradiate on-resonant with an agent, and less efficient de-

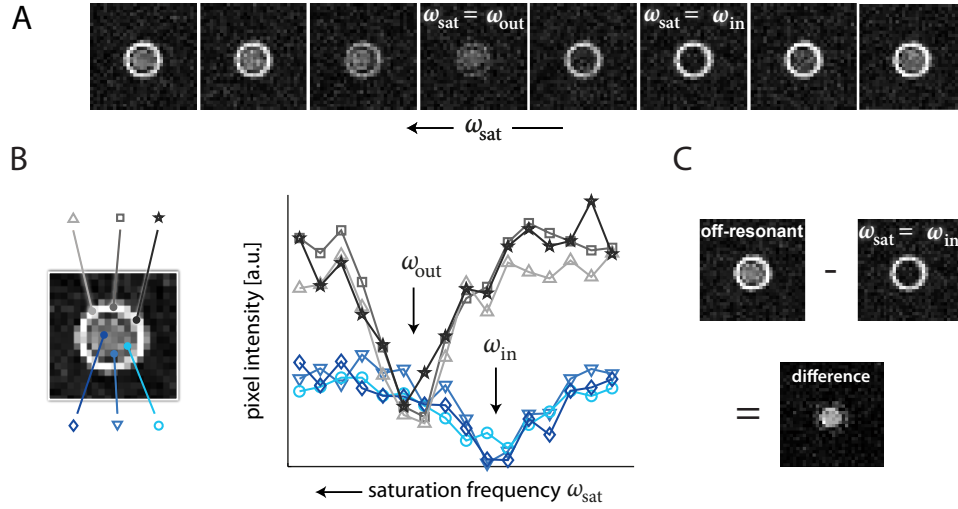


Figure 2.10.: Spectral Hyper-CEST imaging. A: Selected images with different saturation frequencies from a spectral Hyper-CEST image series. The sample tube (see Fig. 2.12) contains a contrast agent in the inner compartment and a different contrast agent in the outer compartment that resonate at NMR frequencies ω_{in} and ω_{out} , respectively. As the saturation frequency approaches either ω_{in} or ω_{out} , the intensity of the respective compartment decreases due to saturation transfer. B: By plotting the intensity of single pixels with respect to the saturation frequency, localized CEST spectra are obtained, similar to the one shown at the bottom of Fig. 2.9B. C: By subtracting one of the images where the saturation frequency was tuned on-resonant with one of the contrast agents (e.g. at ω_{in}), from a reference image without saturation (“off-resonant”), the spatial distribution of that contrast agent can be recovered. The difference image clearly highlights the regions where the corresponding agent was present, in this case the inner compartment.

pletion when we irradiate further off-resonant. However, we now obtain an entire image for each saturation frequency instead of just a single data point, leading to a spectral image series as shown in Fig. 2.10A. In this context, signal depletion is reflected in dark areas in the images. In fact, each pixel in such an image corresponds to an entire CEST spectrum, which can be extracted by plotting the intensity of this pixel against the saturation frequency ω_{sat} (Fig. 2.10B). Just as for CEST spectroscopy, the signal loss for a certain contrast agent can be quantified by subtracting the image acquired with the saturation pulse irradiating on-resonant with this agent from an image either without saturation pulse (2.10C) or with a far off-resonant pulse. Since in the on-resonant image (in this case $\omega_{\text{sat}} = \omega_{\text{in}}$) the signal is depleted in all regions where the agent was present (in this case the inner compartment), the difference image highlights exactly those regions and hence represents a map of the spatial distribution of the contrast agent. The so called CEST effect, which is calculated by dividing the difference image pixel-wise by the image without saturation pulse, displays the relative signal loss due to CEST for all the pixels, and is commonly used for the localization of (Hyper-)CEST contrast agents.

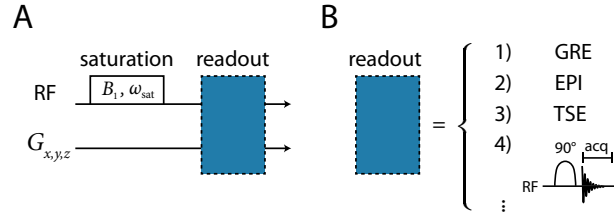


Figure 2.11.: Composition of a typical (Hyper-)CEST sequence. A: After application of an RF saturation pulse with power B_1 at a frequency ω_{sat} , the remaining magnetization is read out. B: The readout can be an imaging sequence (1-3, see section 2.1.6) or a simple spectroscopic readout (4) consisting of a 90° excitation pulse followed by the acquisition of the FID (see Fig. 2.1).

To summarize, a CEST scan consists of a saturation pulse and the subsequent readout of the remaining magnetization (Fig. 2.11). Two CEST scans (an on- and an off-resonant one) are required to detect the presence and – if an imaging readout was applied – the spatial distribution of a certain agent. Multiple CEST scans at different saturation frequencies allow for CEST spectroscopy, which is not only useful if more than one agent shall be detected, but also necessary to extract relevant parameters about these agents, as we will see in the next paragraph.

Mathematically, CEST experiments can be described by extending the Bloch equations (2.6) with exchange terms to the *Bloch-McConnell equations* [91, 92], a set of coupled first-order linear differential equations. For a two pool model considering the Xe@sol (index s) and the Xe@cage (index c) pool and a continuous wave (cw) saturation pulse irradiating with field strength $\omega_1 = \gamma B_1$ along the x -axis, they read

$$\begin{aligned}
 \frac{dM_x^s}{dt} &= \Delta\omega_s M_y^s - R_2^s M_x^s & -k_{sc} M_x^s + k_{cs} M_x^c \\
 \frac{dM_x^c}{dt} &= \Delta\omega_c M_y^c - R_2^c M_x^c & -k_{cs} M_x^c + k_{sc} M_x^s \\
 \frac{dM_y^s}{dt} &= -\Delta\omega_s M_x^s - R_2^s M_y^s & -k_{sc} M_y^s + k_{cs} M_y^c - \omega_1 M_z^s \\
 \frac{dM_y^c}{dt} &= -\Delta\omega_c M_x^c - R_2^c M_y^c & -k_{cs} M_y^c + k_{sc} M_y^s - \omega_1 M_z^c \\
 \frac{dM_z^s}{dt} &= -R_1^s (M_z^s - M_0^s) & -k_{sc} M_z^s + k_{cs} M_z^c + \omega_1 M_y^s \\
 \frac{dM_z^c}{dt} &= -R_1^c (M_z^c - M_0^c) & -k_{cs} M_z^c + k_{sc} M_z^s + \omega_1 M_y^c \quad ,
 \end{aligned} \tag{2.25}$$

where $M_{x,y,z}^{s,c}$ are the components of the magnetization vector in either of the two pools, $\Delta\omega_{s,c} = \omega_{\text{sat}} - \omega_{s,c}$ is the difference between the saturation pulse frequency and the frequency of the either of the two pools, $R_{1,2}^{s,c} = \frac{1}{T_{1,2}}$ are the

relaxation rates, and $k_{cs,sc}$ are the exchange rate constants from one pool to the other. The colored terms in the above equations represent modifications to the conventional Bloch equations. In order to extract e.g. the exchange rate constants from experimental data, measured CEST spectra can be either fitted to the above equations (by evaluating them numerically using e.g. matrix exponentials [92, 93]) or instead, to an analytical approximation (describing the shape of Hyper-CEST spectra as the exponential of a Lorentzian line shape [94]). While the resonance frequency ω_c of a Hyper-CEST contrast agent can be easily obtained from a single CEST spectrum, reliable results for parameters such as the exchange rate constants often require global fitting of multiple spectra at e.g. different saturation powers [95]. Those parameters are especially useful for the screening or the design of new CEST contrast agents, since they characterize the efficiency of these agents.

All concepts described in this section are also valid for conventional CEST detection with thermally polarized nuclei, e.g. protons [33] (this is why “Hyper” in Hyper-CEST was put into brackets in the heading). The major difference to Hyper-CEST is that for thermally polarized nuclei, the initial magnetization recovers again after it has been saturated, since T_1 relaxation drives it back to its thermal equilibrium (compare section 2.2.1). Therefore, the NMR signal has to be acquired quickly (much faster than T_1) to capture the magnetization in its saturated state. For hyperpolarized xenon, the initial hyperpolarized magnetization does not recover once it has been saturated, such that the saturated state persists. However, this includes that fresh hyperpolarized xenon has to be delivered to the sample prior to the next measurement.

2.4. Experimental setup

The experimental setup for all experiments of this work involving hyperpolarization is depicted schematically in Fig. 2.12. Using the pressure from the gas bottle regulator (ca. 3.5 bar overpressure) a gas mixture containing xenon is guided to a custom-designed polarizer operating in continuous flow mode. After hyperpolarization, the gas is transferred into the phantom inside the MR scanner (Avance 400, 9.4 T, Bruker, Germany) and bubbled into the sample solution. It then leaves the magnet through a flow controller and is released to the environment. After a certain time of bubbling – typically 10 to 20 seconds until the solution is saturated – the gas flow is stopped and a measurement is taken after a small waiting time (to allow remaining bubbles to collapse). Subsequently, fresh hyperpolarized xenon is bubbled into the sample again to prepare for the next measurement. The gas flow rate as adjusted by the flow controller is usually around one tenth of a standard liter per minute. The phantom itself is depicted on the left side of Fig. 2.12. It basically consists of a glass tube with an inner diameter of 10 mm containing the sample, and glass capillaries that extend from the gas inlet into the sample

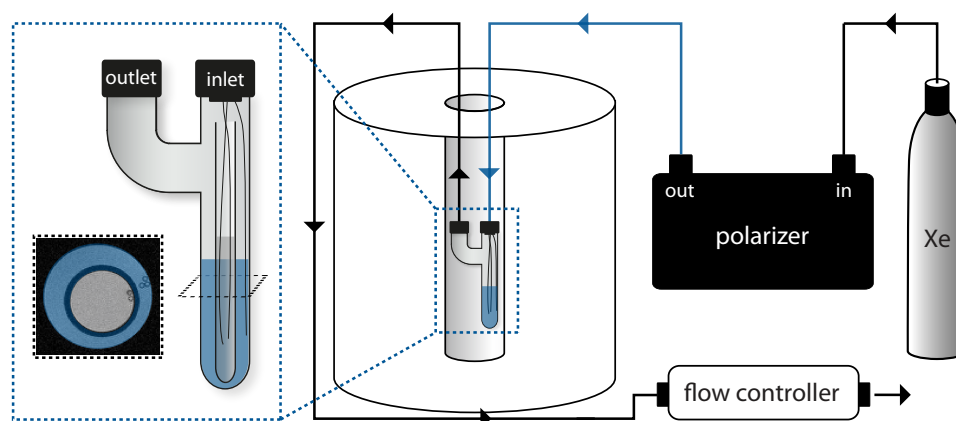


Figure 2.12.: Schematic of the experimental setup for Hyper-CEST experiments. After hyperpolarization, xenon gas is guided into the NMR scanner and bubbled into the sample solution. The insert on the left side depicts the bubbling phantom with two compartments in more detail. The axial slice acquired with conventional proton MRI clearly shows the two compartments and the five glass capillaries through which the gas is delivered to the sample solution. By removing the inner glass tube, the phantom can be used with a single compartment.

solution to deliver xenon gas via bubbling. By optionally inserting another 5 mm NMR tube into the phantom (as shown in the schematic), two different samples can be investigated at a time.

Contents of this thesis

When I started working on this PhD project in 2011, the fastest reported Hyper-CEST image acquisition for xenon biosensors took more than 20 minutes [24] (biosensor concentration approximately $5\ \mu\text{M}$), had a rather small matrix size of 8×8 pixels and required multiple, very stable xenon re-deliveries – conditions which might be problematic especially for future *in vivo* applications. Moreover, the acquisition of CEST spectra, which is e.g. relevant for detecting multiple different sensors simultaneously and for the screening of new contrast agents, was very time consuming, since each point in the spectrum required a separate NMR scan. The goal of this thesis was to overcome or at least diminish these restrictions. It is therefore divided into the following two main projects:

1. **Optimizing Hyper-CEST imaging:** The aim of the first project was to make Hyper-CEST MR imaging faster, more sensitive, and less prone to an unstable xenon delivery. To this end, we initially focused on the spatial encoding of the magnetization: We implemented fast single-shot encoding techniques which efficiently use up the available hyperpolarization for image generation. In combination with an optimized polarizer setup, it was possible to drastically increase speed and sensitivity of Hyper-CEST MRI (imaging of a contrast agent with a concentration as little as $250\ \text{nM}$ in about 100 seconds) [P1]. Applications included the fast acquisition of spectral Hyper-CEST image data sets to discriminate between two different agents, dynamic monitoring of agent diffusion [P1], the first live-cell tracking performed with xenon MRI agents [P6] as well as the first imaging of cell-targeted xenon biosensors [29, 30]. Additionally, we developed a clever signal encoding strategy termed smashCEST (“smash” stands for “shared magnetization after single hyperpolarization”), that allowed us to encode Hyper-CEST images in less than a second using only a single xenon delivery [P1]. In addition to a faster image acquisition, this enabled us to apply Hyper-CEST also in situations where a stable xenon delivery could not be guaranteed.

Next, the observation that a set of spectral Hyper-CEST images contains a lot of redundant information led us to an additional approach for increasing sensitivity. Realizing that the essential features of the entire image set can be described by only a few principal components,

we could improve the image quality in two ways [P2]: (1) by employing principal component analysis (PCA) based post-processing, we could remove much of the noise in the data, and (2) by acquiring less raw data than actually required by the Nyquist sampling criterion, we could distribute the available hyperpolarized magnetization among less data points, hence increasing the signal per data point. To still be able to reconstruct meaningful images from the sub-sampled data set, we used an iterative algorithm exploiting the aforementioned redundancies. As approach (1) decreases the noise and approach (2) increases the signal, both lead to an enhanced signal-to-noise ratio (in total, we achieved a 4.9-fold increase of SNR for the image data set used in our study).

2. **Accelerating (Hyper-)CEST spectroscopy:** In the second project, we aimed at reducing the acquisition time of Hyper-CEST spectra for *in vitro* experiments, which is e.g. important for the screening or the study of new contrast agents or other host-guest complexes, for detecting multiple agents or substances simultaneously, and for the monitoring of dynamic processes. We therefore employed a novel frequency encoding strategy for CEST that is based on magnetic field gradients instead of a frequency sweep [96]. It therefore allowed us to acquire an entire CEST spectrum with only two NMR scans (conventionally, one requires one scan per data point in the spectrum). We initially implemented and improved this technique for conventional ^1H CEST agents (reducing scan time by a factor of up to 300) [P3], and then modified it for the use with hyperpolarized xenon (reducing scan time by a factor of up to 40) [P4]. The latter enabled us to dynamically monitor an enzymatic reaction using Hyper-CEST spectroscopy. We furthermore showed that the above-mentioned new frequency encoding strategy can also be extended with imaging capabilities by using a fast multi-slice readout [P5]. This approach, termed ultrafast CEST imaging, combines aspects from publications [P2] and [P3] and can be e.g. used to rapidly screen multiple CEST agents in multiple sample tubes simultaneously.

In the following, I summarize these projects in more detail. Each subsection corresponds to one of the journal articles I authored [P1-P5]. An overview of all publications related to this work can be found in the “List of publications” on page 65, where I also accurately specify my contributions to each project.

3.1. Optimizing Hyper-CEST imaging

In this section, I outline how we improved Hyper-CEST imaging by using clever image acquisition and post-processing techniques.

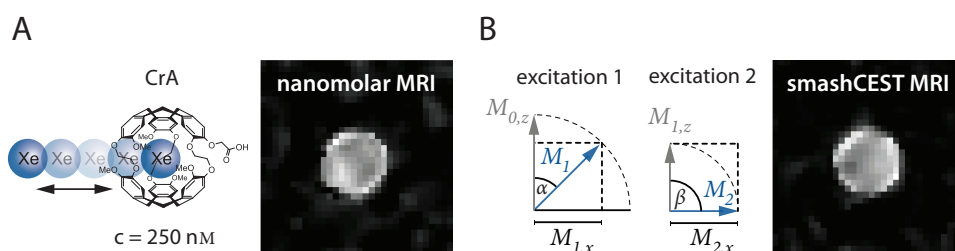


Figure 3.1.: Improved Hyper-CEST imaging using a single-shot EPI sequence. Imaging nanomolar agent concentrations (A) and encoding CEST images in less than a second using smashCEST with a single xenon delivery (B). The images show the spatial distribution of the contrast agent (in this case Cryptophane-A) in an axial slice of the phantom (see Fig. 2.12, left).

3.1.1. Single-shot Hyper-CEST MRI

— corresponding to publication P1

The first paper, which represents a collaborative work between my colleague Martin Kunth and me [P1], contained two major improvements for Hyper-CEST imaging (schematically depicted in Fig. 3.1):

1. The use of a single-shot EPI sequence (compare Fig. 2.5B) allowed us to record an entire CEST-weighted image using only a single excitation pulse and a single saturation preparation. This not only speeds up the measurement, but also efficiently uses the available hyperpolarized magnetization for data acquisition. Compared to the then state-of-the-art Hyper-CEST imaging strategy employing chemical shift imaging (detecting $5\text{ }\mu\text{M}$ contrast agent in 22 min using an 8×8 matrix with a voxel size of $1.5 \times 1.5 \times 10\text{ mm}^3$ [24]), we achieved a more sensitive detection in much less time (detecting 250 nM contrast agent in 102 s using an 32×32 matrix with a voxel size of $0.6 \times 0.6 \times 20\text{ mm}^3$). One prerequisite for this technique is the availability of enough initial hyperpolarized magnetization for single-shot imaging, which the optimized polarizer in our lab perfectly fulfills.
2. The use of two different excitation flip angles (45° - 90°) allowed us to acquire a Hyper-CEST image with only a single xenon delivery (termed smashCEST, shared acquisition after a single hyperpolarization). This technique not only further accelerates image recording (image encoding: 940 ms, total acquisition time including xenon delivery: 29 s), but also makes Hyper-CEST independent from a stable xenon re-delivery: The hyperpolarized xenon from only a single delivery is used to generate both the off- and the on-resonant image required for CEST (see [P1], Supporting Information, Fig. S4). This is important, since many polarizer setups do not necessarily guarantee a stable xenon supply for multiple acquisitions (especially for *in vivo* experiments [28]). In the

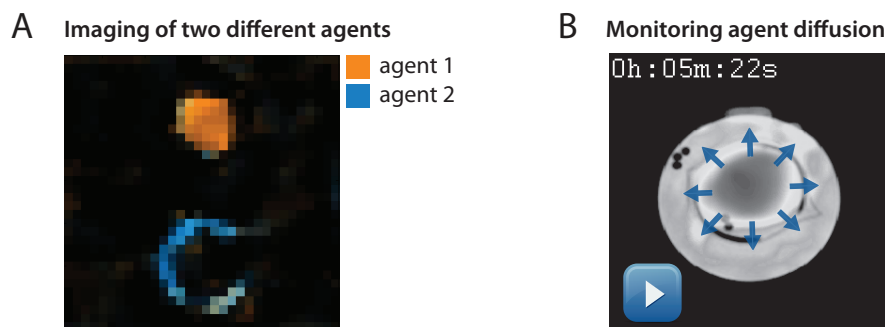


Figure 3.2.: Applications of fast Hyper-CEST using an EPI sequence. A: The acquisition of spectral Hyper-CEST images allowed us to detect and visualize the spatial distribution of two contrast agents, here displayed in different colors. B: Movie showing the diffusion of contrast agent molecules through a dialysis tubing as observed with Hyper-CEST by taking an image every 33 s. If the movie is not displayed correctly, try to open this document with Adobe Acrobat Reader.

original Hyper-CEST approach [24], the acquisition of a single CEST image required as many as 64 stable xenon re-deliveries.

These improvements in sensitivity and recording speed allowed us for the first time to acquire entire spectral Hyper-CEST image series in an acceptable time frame of several minutes. With such a combination of spectral and spatial information, multiple different contrast agents can be localized simultaneously. This allows for example the imaging of multiple biochemical targets or biomarkers (multiplexing), which is of great use for e.g. disease detection: Since typically a variety of biomarkers play a role in characterizing a disease [1], detecting multiple markers is likely to lead to a more accurate and reliable diagnosis compared to detecting just a single marker. As a proof of principle, we demonstrated the imaging of two non-targeted Hyper-CEST agents (Cryptophane-A, CrA, in two different solutions) as shown in Fig. 3.2A. The fact that the two agents were separated by only about 1 ppm (131 Hz) in the xenon NMR spectrum highlights the spectral selectivity of the method, allowing for an efficient multiplexing. The shift artifact between the two compartments of our phantom (Fig. 2.12, left) seen here stems from the chemical shift between the two bulk xenon pools as described in publication [P1].

Another new Hyper-CEST imaging application that is enabled by the strongly reduced acquisition times is the monitoring of dynamic processes such as diffusion. To demonstrate this, we inserted a dialysis tubing containing dissolved contrast agent molecules (CrA) into our phantom. By acquiring a Hyper-CEST image every 33 seconds, we were able to observe the diffusion of the contrast agent through the dialysis membrane into the outer compartment (see movie in Fig. 3.2B). This experiment demonstrated the feasibility of time-resolved biosensor uptake studies for future *in vivo* applications.

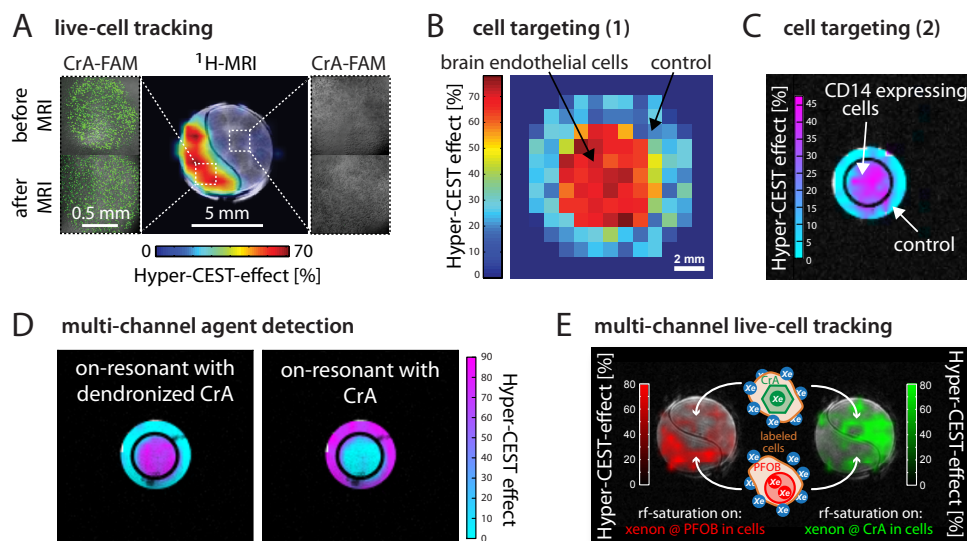


Figure 3.3.: Further studies that used the single-shot imaging sequences we implemented during this work. A: First Hyper-CEST imaging of live cells labeled with Cryptophane-A linked to a fluorescent dye (CrA-FAM) (adapted from [P6]). Intracellular concentration of CrA $\sim 15 \mu\text{M}$. B: Localization of a targeted xenon biosensor (large unilamellar vesicles loaded with CrA and functionalized with lipopeptides) for human brain microvascular endothelial cells (adapted from [29]). Concentration of the contrast agent $\sim 1 \text{ nM}$. C: Targeting cells via surface receptors (in this case CD14) using a modular antibody-based biosensor conjugated to CrA (adapted from [30]). Concentration of the contrast agent $\sim 20 \text{ nM}$. D: Multiplexing between “normal” CrA and a more water-soluble, dendronized version of the contrast agent, demonstrating high spectral selectivity (adapted from [97]). Concentrations $\sim 13 \mu\text{M}$. E: Multi-channel live cell-tracking with high spectral selectivity using Hyper-CEST and two different xenon contrast agents: plain CrA and perfluorooctyl bromide (PFOB) nanodroplets with intracellular concentrations of around $40 \mu\text{M}$ and 80 nM , respectively (adapted from [31]). In A and D, PCA based post-processing as presented in publication [P2] was employed to enhance the images.

While in publication [P1] a single-shot EPI sequence was used, I furthermore adapted a single-shot turbo spin-echo (TSE) sequence (compare Fig. 2.7) for the use with Hyper-CEST. TSE may yield more signal than EPI especially if T_2 is long enough to allow for the acquisition of multiple spin-echoes. We successfully employed the sequence to generate the first live cell-tracking images with hyperpolarized xenon [P6] (Fig. 3.3A) and it was subsequently also used within various other projects of our research group (for examples, see Fig. 3.3B-E and refs. [29–31, 97, 98]). Note that from these, refs. [29] and [30] are the first publications (regarding submission date) that demonstrate imaging of the spatial localization of a cell-targeted xenon biosensor with Hyper-CEST (Shapiro et al. [35] submitted the detection of a cell-targeted xenon biosensor about a month later, using a similar Hyper-CEST TSE imaging sequence).

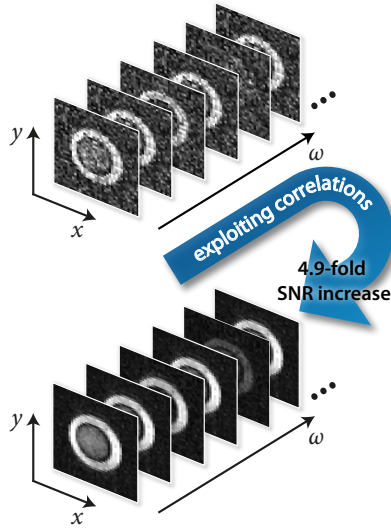


Figure 3.4: Exploiting correlations in the spectral domain to improve image quality.

To summarize, we demonstrated in this section that single-shot sequences such as EPI or TSE are particularly suitable for the fast and sensitive MR imaging of hyperpolarized nuclei with CEST, provided that the initial magnetization is large enough to allow for single-shot detection.

3.1.2. Exploiting redundancies in the spectral domain

— corresponding to publication P2

While we used single-shot MRI to increase speed and sensitivity of Hyper-CEST imaging in the previous section, the approach we pursued in my second publication [P2] is substantially different. Here, the redundant information present in spectral (Hyper-)CEST image series is exploited to increase the signal-to-noise ratio by a factor of up to 4.9 (see Fig. 3.4). To illustrate what these redundancies consist of, an example of a spectral CEST image stack is shown in Fig. 3.5A. Just by visual inspection of this image series it becomes evident that the data is indeed highly redundant: Each image basically contains the same structure, except that some regions get darker or brighter as the saturation frequency ω_{sat} changes. In other words, many pixels vary in a similar fashion as a function of ω_{sat} , as pointed out in Fig. 3.5B (for instance, the pixels in the outer compartment all decrease in intensity as ω_{sat} approaches $\omega_{\text{out}} = 79.5$ ppm).

In order to exploit these pixel correlations, we proposed two compatible methods. The first one filters the noise in the data and is applied as a post-processing step. It is based on principal component analysis (PCA), a commonly used tool to discover and utilize correlations in data [99]. The second technique utilizes the redundancies directly at the level of image acquisition by recording only a fraction of the conventionally required data points in k -space (sub-sampling) and thereby increasing the signal per data point. It is re-

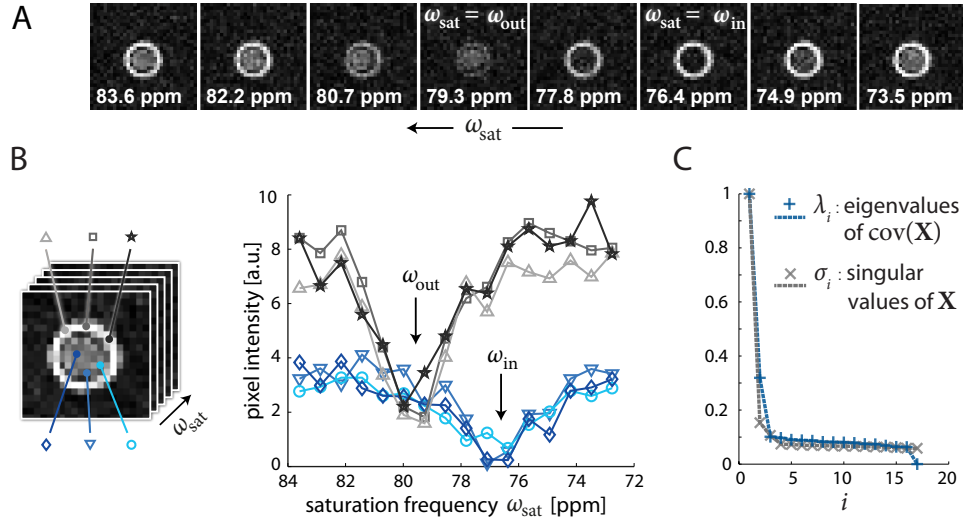


Figure 3.5.: Illustrating the redundancies in a spectral CEST image series (partly adapted from Fig. 2.12). A: Selected images from a spectral Hyper-CEST image series, the saturation frequency is denoted on the bottom of each image (the full data set can be found in [P2], Supporting Information, Fig. S3). The phantom (see Fig. 2.12) contains two different contrast agents in the inner and the outer compartment that resonate at NMR frequencies ω_{in} and ω_{out} , respectively. B: Plotting the intensities of single pixels with respect to the saturation frequency reveals a high degree of correlation for pixels located in the same compartment. C: The redundancy in the data is further illustrated by principal component analysis (PCA) and singular value decomposition (SVD): (1) A small number of the eigenvalues λ_i of the covariance matrix of the data set \mathbf{X} and (2) a small number of the singular values σ_i of \mathbf{X} are much larger than all the others, indicating that only a few principal components convey most of the relevant information. Fig. 3.6 shows how the 2D matrix \mathbf{X} is generated from the spectral Hyper-CEST image series.

lated to the first inasmuch as it takes advantage of the very same correlations to correctly reconstruct the full images from the subset of measurements.

PCA-based denoising

Principal component analysis deconstructs the data set under investigation into its principal components (PCs) – a set of new, uncorrelated variables – and ranks them according to how much of the data’s variance they describe. The plot in Fig. 3.5C shows that most of the data variance in our spectral Hyper-CEST image series can actually be described by only the first two principal components, underlining the high degree of correlation (λ_i is the portion of the variance that is described by the i -th principal component). Further analysis additionally indicated that all lower ranked PCs contained mostly only noise (see Fig. 2b in [P2]). Therefore, by reconstructing the entire data set using only the first two PCs, we could remove much of the noise and increase the SNR of the spectral images by a factor of 2.2. This post-processing technique can be used to enhance the images of any spectral

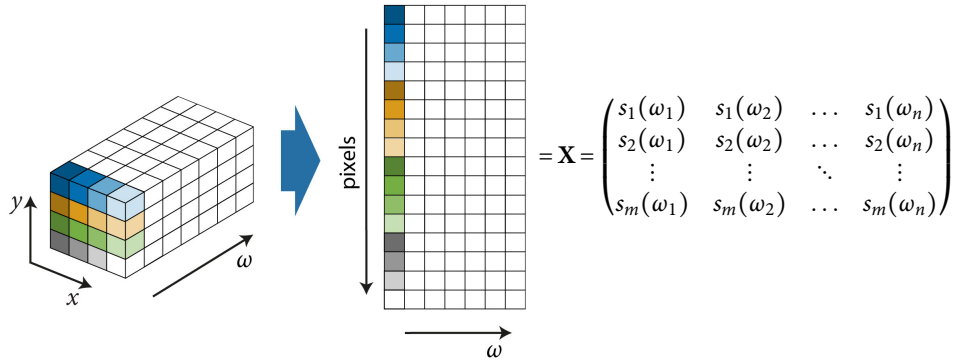


Figure 3.6.: Preparing the spectral Hyper-CEST image stack for PCA or SVD. Usually PCA and SVD are calculated for 2D matrices. Our spectral Hyper-CEST image stack, however, has naturally the form of a 3D matrix consisting of n images (i.e. 2D matrices) associated with n different saturation frequencies $\omega_1, \dots, \omega_n$ (left). We therefore reshape each single image containing m pixel intensities $s_i(\omega_j)$ into a column vector, and then put the resulting column vectors together in a $m \times n$ 2D matrix \mathbf{X} (right). Note that here the saturation frequencies are denoted as ω and not as ω_{sat} in the interest of clarity.

CEST data set exhibiting correlations, no matter if hyperpolarized nuclei or thermally polarized ^1H nuclei are detected. It has also been successfully applied in other projects of our group (see publication [P6], ref. [97] and Fig. 3.3A and D).

Realizing that most of the acquired data in spectral CEST imaging is actually redundant, it seems natural to ask if it is at all necessary to acquire all of the data. The main aspect of the next subsection is therefore to further utilize the redundancies already at the stage of image acquisition by sub-sampling k -space.

Sub-sampled image acquisition

In conventional MRI, recording less data than required by Nyquist sampling theory (see section 2.1.5 and Eq. 2.22), commonly referred to as sub- or undersampling, is usually used to reduce the scan time [100]. Here however, we mainly aim at increasing the MRI signal and thereby the sensitivity. How can this be achieved by acquiring less data?

When hyperpolarized nuclei are involved – in contrast to thermally polarized samples – the magnetization does not relax back to its initial, hyperpolarized magnitude M_0 once it has been excited into the transverse plane for signal acquisition (see section 2.2.1). Hence, every data point acquired in k -space for image generation uses up a certain fraction of M_0 . It is therefore evident that the fewer data points or k -values are acquired, the higher the fraction of magnetization available for each data point, and hence the higher the signal for each data point. We therefore proposed that sub-sampling could potentially increase the signal in Hyper-CEST MRI.

PCA, singular values, and matrix rank

How are these three terms related?

- The first step for performing PCA on a 2D matrix \mathbf{X} with n rows is to subtract the mean of each single row from that row (mean-centering), and then calculating the covariance matrix $\text{cov}(\tilde{\mathbf{X}}) = \frac{1}{n-1} \tilde{\mathbf{X}} \tilde{\mathbf{X}}^T$ of the obtained mean-centered matrix $\tilde{\mathbf{X}}$. The *eigenvalues* λ_i of $\text{cov}(\tilde{\mathbf{X}})$ describe how much of the variance of the data in \mathbf{X} can be described by the i -th principal component.
- The *singular values* σ_i , on the other hand, are strongly related to the λ_i since they are given by the square-root of the eigenvalues of $\mathbf{X} \mathbf{X}^T$.
- Finally, the *rank* of a matrix is given by the number of non-zero singular values of that matrix. Hence, a matrix with low rank has a small number of non-zero singular values σ_i , and hence also small number of non-zero λ_i (i.e. a small number of significant principal components).

However, if sub-sampled MRI data is reconstructed the usual way by Fourier transform (FT), artifacts occur (see Fig. 2.4 and [P2], Fig. 3a) due to violation of the Nyquist criterion. We therefore incorporated a more sophisticated iterative reconstruction algorithm [101], that uses the redundancies described in the previous section as prior knowledge to recover meaningful images from the sub-sampled data (see Fig. 3.7). In particular, it assumes that the data matrix \mathbf{X} is approximately low rank, i.e. has a small number of significant singular values σ_i , which is shown in Fig. 3.5C to be a valid assumption for our data set (see also box on this page).

Employing the described sub-sampling, we achieved a signal gain by a factor of 2.5 when using a conventional gradient-echo acquisition (see section 2.1.6) together with a variable excitation flip angle as described in ref. [89]. The variable flip angle ensures that each gradient-echo (i.e. each line in k -space) has the same amount of initial transverse magnetization [P2]

$$M_{\perp} = \frac{M_0}{\sqrt{n}} \quad , \quad (3.1)$$

where n is the total number of k -space lines or phase-encodings. This guarantees a very homogeneous coverage of k -space, which minimizes image artifacts. Eq. 3.1 also shows clearly that the less lines are acquired in k -space, i.e. the higher the degree of sub-sampling, the more magnetization M_{\perp} per line is available. If however too few lines are acquired, then the iterative algorithm fails to correctly reconstruct the images, such that a trade-off must

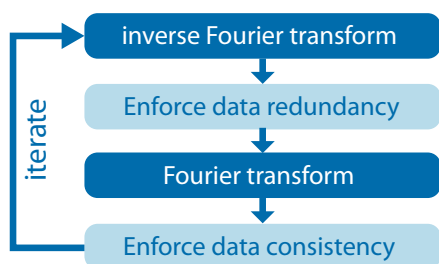


Figure 3.7: Diagram of the iterative algorithm used for image reconstruction. Starting with an initial guess (in Fourier space), the data is Fourier transformed into image space, and data redundancy is enforced by singular value shrinkage [101]. Then, the resulting image data is transformed back into Fourier space, and consistency with the measured raw data is enforced.

be found. Note also that image reconstruction works best when the sampled data points are distributed in a random fashion in sampling space, such that the folding artifacts become incoherent (see Fig. 2.4E and refs. [100, 102]). The sampling pattern we employed is depicted in Fig. S4 of the Supporting information of publication [P2].

On top of performing sub-sampling, we could then also apply PCA on the reconstructed data set as described in the previous section. As this additionally removed some of the noise in the data, we achieved an overall gain in SNR of 4.9 (see Fig. 3.4).

We furthermore observed that the single-shot sequences EPI and TSE discussed in the previous section did not benefit from sub-sampling, since they use the available hyperpolarization already very efficiently. However, they are more prone to artifacts such as ghosting (EPI) or blurring (TSE) than the gradient-echo sequence used here.

To summarize, we demonstrated the presence of redundancies in typical spectral Hyper-CEST image series and proposed two methods to exploit these for improving sensitivity: PCA-based post-processing and sub-sampled data acquisition.

3.1.3. Summary (for optimized spatial encoding)

In this first project of my thesis, we investigated and developed various tools to tackle previous limitations of Hyper-CEST imaging regarding sensitivity and encoding speed that are applicable under various conditions: (1) Single-shot imaging with either EPI or TSE sequences to efficiently use the available hyperpolarization and to increase encoding speed, (2) sub-sampled imaging using a variable flip angle to increase the signal per data point within a gradient-echo readout, (3) PCA-based post processing to reduce image noise, and (4) smashCEST to make Hyper-CEST independent of a stable xenon delivery.

When the NMR signal of hyperpolarized xenon is strong enough to allow for single-shot image acquisition, we propose to use the Hyper-CEST EPI (for short T_2) or TSE (better for longer T_2 and less prone to ghosting artifacts) sequences employed in publications [P1] and [P6], enabling fast and

efficient use of the available magnetization. Utilizing these sequences paved the way for new Hyper-CEST applications, such as the acquisition of spectral image series for the detection of multiple different agents in an acceptable time frame, or the monitoring of dynamic processes such as contrast agent diffusion. To date, these sequences were successfully used in various projects of our research group [29–31, 97, 98, 103, 104]. When on the other hand the signal decays very rapidly, e.g. due to very short T_2 or T_2^* times, or when a very homogeneous k -space coverage must be achieved (e.g. to avoid blurring artifacts), we suggest a conventional gradient-echo sequence paired with a variable flip angle excitation as proposed in ref. [89] as an alternative. In this context, and when entire Hyper-CEST spectra are imaged, we showed that sub-sampling increases image quality (SNR increase of a factor of 2.5 in our experiment) since the initial magnetization is distributed among less data points and hence a larger fraction of it is available for each data point [P2].

Furthermore, we discovered a high degree of correlation between the pixels of spectral Hyper-CEST image series. This can be exploited not only to correctly reconstruct the above-mentioned sub-sampled image data, but also to perform PCA-based denoising to enhance image quality (SNR increase of a factor of 2.2 in our experiment) [P2]. Since the latter technique only involves a post-processing step, it can be employed to all spectral CEST image stacks independent of the acquisition method. It has been successfully applied in refs. [P6, 97].

As CEST is a difference technique, it always requires the acquisition of at least two data points or images: One with saturation, and one without saturation as a reference (see Fig. 2.10). Both scans must have the same initial magnetization or signal, otherwise the calculated difference is meaningless. In Hyper-CEST, this requires the xenon polarization level and delivery to be very stable, a criterion which our continuous-flow polarizer perfectly fulfills (showing less than 0.56% shot-to-shot noise [87]). However, this condition is likely to be violated for polarizer setups without optimization for continuous flow (e.g. batch delivery and dissolution of xenon gas through shaking of the sample tube [25, 58]), or for *in vivo* experiments [28]. In such a setting, smashCEST might prove very useful, since it allows the generation of Hyper-CEST contrast with only a single delivery of xenon. This not only speeds up the measurement, but also makes it robust against an unstable xenon supply. However, the magnetization of this single delivery has to be shared among two acquisitions, therefore reducing the SNR.

For all methods mentioned above, a high spectral selectivity to distinguish between multiple contrast agents or biosensors resonating at different NMR frequencies can be preserved (e.g. by adjusting the power of the saturation pulse), as for example demonstrated in publication [P1] and refs. [31, 97].

Recalling that the first localized (one-dimensional) NMR experiments

with xenon biosensors took more than two hours [90], and that the first MRI with such sensors using Hyper-CEST took 22 minutes despite a rather low resolution, the results shown here represent another important step towards molecular imaging with xenon Hyper-CEST *in vivo*.

3.2. Accelerating (Hyper-)CEST spectroscopy

Performing (Hyper-)CEST experiments including the spectral dimension allows us not only to detect the presence of multiple different contrast agents or substances as demonstrated in the previous sections, but also gives us access to valuable parameters to characterize these agents: For example, at which NMR frequency they respond, how broad the spectral width of their response is at a specific saturation pulse power, and what the exchange rate constants (which determine the efficiency of the CEST agent) are. These parameters, which are usually extracted by fitting the CEST spectra to models such as the Bloch-McConnell Equations, (Eq. 2.25), enable us for example to figure out whether a given construct is a powerful and efficient CEST agent, to make predictions how this agent will respond at different pulse powers and concentrations and hence to calculate optimal values for those, and to determine which agents can potentially be applied simultaneously in the same organism to allow for the targeting of multiple biomarkers. Altogether, including the spectral dimension gives a more complete picture of the CEST mechanisms within a given system, and is hence important for the characterization or screening of new potential contrast agents, both for CEST and Hyper-CEST.

Even though the results of the previous sections represented a substantial improvement for Hyper-CEST imaging in terms speed and sensitivity, until 2013, the minimum acquisition time for entire Hyper-CEST spectra was still limited by the inherent requirement of a separate scan with a different saturation frequency for each data point in the spectrum – including a separate delivery of hyperpolarized xenon, which takes typically 10 to 20 seconds, plus the application of the saturation pulse, which takes typically around 5 to 15 seconds. Assuming that we wanted to acquire a Hyper-CEST spectrum consisting of say 40 data points (the spectral resolution must be sufficiently high to obtain reliable fitting results), one would therefore end up with an acquisition time of at least 10 minutes per spectrum. Note that this is not only true for Hyper-CEST, but also for conventional CEST with thermally polarized protons: Here, again the saturation pulse length and furthermore the waiting time to allow the magnetization to recover (typically around a couple of seconds, depending on T_1), again enforces rather long scan times for an entire CEST spectrum.

With this in mind, if one wanted to screen an entire library of different contrast agent constructs (note that even small chemical modifications within a

construct can dramatically change its CEST properties), presumably including spectral CEST measurements for different saturation pulse powers, agent concentrations and in different solvents, it becomes evident that a reduction in acquisition time would be highly desirable to be able to perform all the necessary experiments in an acceptable time frame. In addition, a faster acquisition would allow for the monitoring of dynamic processes using Hyper-CEST spectroscopy.

To overcome the inherent requirement of a separate scan per spectral data point, we implemented a novel frequency encoding approach for CEST first published by Xu et al. [96] from the group of Alexej Jershow (we were working on this approach simultaneously without being aware of their work, and published our results, including some improvements, a couple of month later [P3]). The key idea is to encode the saturation frequency with magnetic field gradients along a spatial direction instead of sweeping it from scan to scan.

Fig. 3.8 shows a more detailed description of that principle: We first consider a homogeneous sample of nuclear spins with the shape of a cuboid (Fig. 3.8A). If no gradient is applied, all spin packets precess the same Larmor frequency ω , here arbitrarily set to zero. The blue line in the bottom of Fig. 3.8A shows the magnetization $M_0^{\text{proj}}(x)$ of the sample with respect to the x -axis, or in other words, it shows the projection of $M_0(\mathbf{x})$ onto the x -axis. As the sample is homogeneous, this projection is constant, i.e. each slice of the sample along the x -axis carries the same amount of magnetization. If a saturation pulse is applied at $\omega_{\text{sat}} = 0$, it will saturate the magnetization of the sample. Since all spins in the sample precess at the same frequency, the saturation will affect the magnetization of all the slices in the same way, that is, the projection of the magnetization $M_0^{\text{proj}}(x)$ after saturation (S_{on} , gray line) will be again constant, but have a smaller magnitude than without saturation (S_{off}). This is the conventional saturation effect. Next, suppose that a gradient \mathbf{G}_c (henceforth called the CEST gradient) with magnitude G_c is switched on, pointing into a direction along which the sample is homogeneous (assume for example that \mathbf{G}_c points into the x -direction as in Fig. 3.8B). The spatially varying magnetic field causes the spin packets to now precess at different frequencies depending on their location, or more precisely, on the projection of their position vector \mathbf{x} onto \mathbf{G}_c (compare Fig. 2.3 and Eq. 2.16). While this has no implication on S_{off} , i.e. the projection of the magnitude of the magnetization when no saturation is applied (the gradient only changes the precession speed of the spin packets, but not their magnetization magnitude) the effect of the saturation pulse (again applied at $\omega_{\text{sat}} = 0$) now substantially changes: Only the central y - z slice of the sample, where the additional magnetic field induced by the CEST gradient is zero and hence the precession frequency $\omega = 0$, will experience the same on-resonant saturation that the entire sample experienced in 3.8A without the gradient. The further the slices are away from the center, the stronger ω deviates from zero and hence the

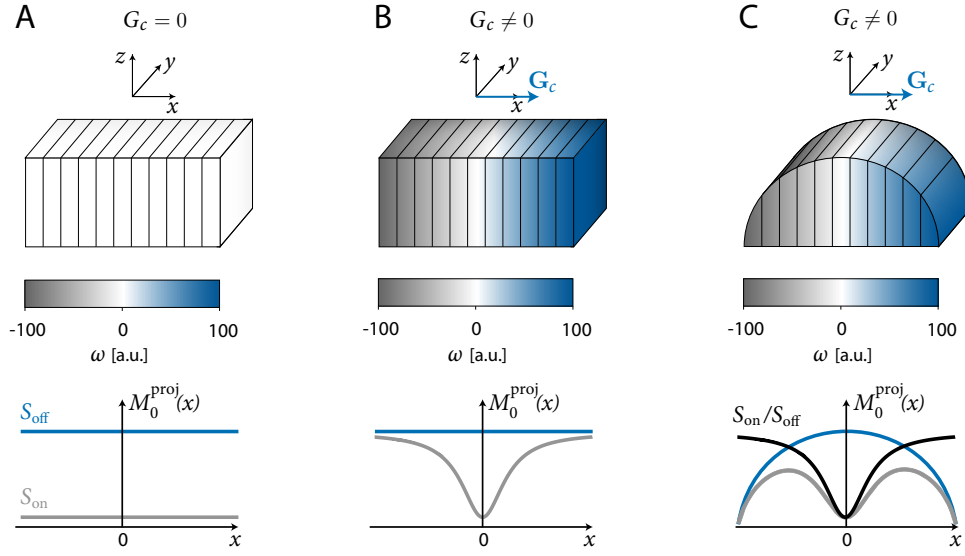


Figure 3.8.: Principle of ultrafast CEST spectroscopy (UCS). The top row shows the magnetic field gradient vector G_c and below it the sample, and the bottom row shows the projection of the sample's magnetization with (S_{on}) or without (S_{off}) saturation pulse. A: No CEST gradient is applied. B: The CEST gradient establishes different off-resonant conditions for the saturation pulse along the x -axis. Hence S_{on} is equivalent to a CEST spectrum. C: If the shape of the sample is not homogeneous, S_{on} can be divided by S_{off} to recover the CEST spectrum.

more off-resonant is the saturation they actually undergo. It is plausible that thus the projection S_{on} represents an entire CEST spectrum, encoded along the spatial direction of the CEST gradient using only a single saturation pulse within a single scan. In contrast to conventional CEST, here, the off-resonant data points in the spectrum are not generated by acquiring additional scans where the saturation frequency is tuned to different off-resonant values, but by a gradient-induced change of the Larmor frequencies of the nuclei in the sample, such that they experience the saturation with different off-resonance conditions depending on their position.

While the sample must be homogeneous in the direction of the CEST gradient to ensure that the described method yields reliable CEST spectra, it is not required that the sample has a homogeneous shape: An irregular shape along the CEST gradient direction (see Fig. 3.8C) can be compensated for by acquiring an additional scan with the saturation pulse turned off (see S_{off} , blue curve) to obtain a 1D projection of the object of interest. Dividing the CEST-weighted scan S_{on} by S_{off} , the geometry-related effects vanish and the pure CEST effect can be recovered.

In summary, the described method, henceforth called ultrafast CEST spectroscopy referring to ref. [96], in principle allows to acquire an entire CEST spectrum using only two NMR scans: One with saturation, S_{on} and one with-

out, S_{off} (how these scans are acquired is described in the following subsection). While the idea for this method had already been published for CEST [96] and in fact had been reported much earlier for magnetization transfer (MT) [105], we focused on improving it and adapting it to Hyper-CEST, as discussed in the next subsections: (1) We improved the method by including slice selection and applied it for the first time to monitor dynamic processes in proton CEST [P3], (2) we successfully transferred and adapted the method to experiments with hyperpolarized nuclei (Hyper-CEST) [P4] and (3) we extended this (initially purely spectroscopic) technique with imaging capabilities, allowing for the simultaneous investigation of multiple samples at the same time (ultrafast CEST imaging [P5]).

3.2.1. Improved ultrafast CEST spectroscopy

— corresponding to publication P3

Before adapting ultrafast CEST spectroscopy (UCS) to Hyper-CEST, we applied it to conventional proton CEST [P3] first (this was done due to the simpler experimental handling). We therefore developed the pulse sequence shown in Fig. 3.9A, which can be very easily derived from the CEST-weighted gradient-echo imaging sequence already mentioned in the background chapter (Fig. 2.11 with the GRE readout displayed in Fig. 2.5A). The additional modifications include:

1. The application of a CEST gradient G_c along the read direction during the saturation pulse, which is the crucial element of UCS as discussed in the previous section,
2. Switching off the phase-encoding, so that the read gradient switched on during recording guarantees the acquisition of the projection of the magnetization (see box on page 48).

We validated the UCS sequence on the basis of the proton CEST contrast agent Eu-DOTA-4AmC (see [P3], Supporting Information, Fig. S4), which resonates at ~ 50 ppm upfield from the bulk water resonance at room temperature. We dissolved the agent in water and filled the solution into a conventional 10 mm NMR tube. Fig. 3.9B shows an overview MRI scan of the sample together with the scan geometry for UCS. We then ran the UCS sequence in Fig 3.9A twice, once with and without saturation pulse to obtain the projections S_{on} and S_{off} , which took in total 34 seconds. By dividing the two, we could recover the ultrafast CEST spectrum (Fig. 3.9C, black curve), which clearly shows the resonance from the CEST agent at around 50 ppm as expected. For validation, we additionally acquired a CEST spectrum the conventional way by sweeping the saturation pulse (total acquisition time: 20 min), which showed excellent agreement to the one acquired with UCS

How to obtain the projection of a sample

The projection of a sample along a spatial direction can be easily obtained by switching on a gradient in that direction during the signal readout. Recall from Eq. 2.20 that the NMR signal, after tipping the magnetization with magnitude M_0 into the transverse plane with a 90° RF pulse, and in the presence of a gradient, reads

$$S(\mathbf{k}) \propto \int M_0(\mathbf{x}) e^{-i\mathbf{k} \cdot \mathbf{x}} d\mathbf{x} = \int_x \int_y \int_z M_0(x, y, z) e^{-i\mathbf{k} \cdot \mathbf{x}} dz dy dx ,$$

where \mathbf{k} depends on the gradient strength and the duration it has been switched on. If the gradient is e.g. applied along the x direction, this simplifies to

$$S(k_x) \propto \int_x e^{-ik_x x} \underbrace{\int_y \int_z M_0(x, y, z) dz dy}_{M_0^{\text{proj}}(x)} dx ,$$

where the exponential has been written outside the y and z integration, since it does only depend on x . By sampling $S(k_x)$ sufficiently densely (see the Nyquist criterion Eq. 2.22), the projection of the sample magnetization can be obtained by an 1D inverse Fourier transform:

$$M_0^{\text{proj}}(x) \propto \int S(k_x) e^{ik_x x} dk_x .$$

(see [P3], Supporting Information, Fig. S1). Ultrafast CEST spectroscopy is hence suitable to acquire reliable CEST spectra in much less time compared to conventional CEST. Note that in the implementation of Xu et al. [96], the FID was recorded, whereas our UCS sequence acquires a full gradient-echo, which theoretically leads to an SNR increase by a factor of 2 [106, Table 2.5], if T_2 and T_2^* are much longer than the read dephasing and the acquisition time.

We then utilized the highly accelerated acquisition of CEST spectra to dynamically monitor induced temperature changes in our sample with sub-minute resolution. When the temperature changes, the chemical shift of the CEST resonance usually changes as well. For many CEST agents, especially for europium(Eu)-based complexes as used here, this chemical shift is approximately linear with temperature [107–110]. We therefore used the chemical shift, as extracted from the CEST spectra, as an indicator for temperature changes. To artificially induce such a temperature change, we set the variable temperature unit (VTU) of our NMR scanner that regulates the sample temperature with a temperature-controlled air flow to different target

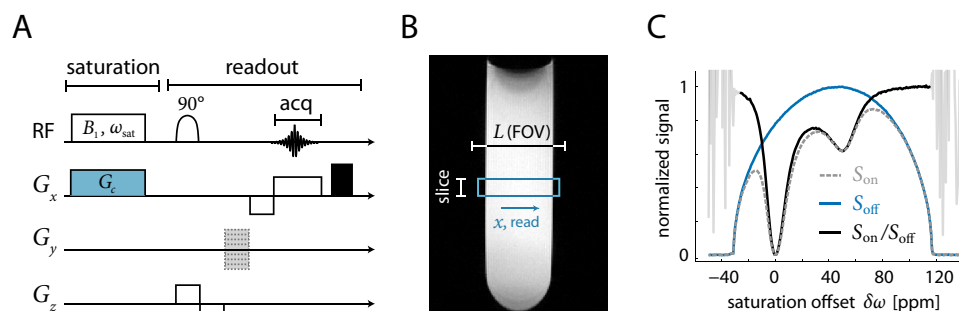


Figure 3.9.: Ultrafast CEST spectroscopy with protons. A: UCS sequence diagram, derived from a gradient-echo sequence (Fig. 2.5A). Additional elements are depicted in blue, and removed elements (phase-encoding) are depicted in light gray. B: Geometry of the UCS scan depicted on an ^1H overview image. The CEST gradient G_c is applied along the x or read direction. C: UCS signals S_{on} , S_{off} and their ratio, constituting the CEST spectrum. The strong noise at the edges of this spectrum stem from the division operation at regions where S_{off} is close to zero.

values while continuously acquiring CEST spectra every 34 s using UCS. Fig. 3.10 shows a movie of the resulting CEST spectra: First, the sample is cooled down to 278 K and then heated up to 313 K by the VTU. It can be seen that not only the chemical shift difference between the bulk water pool at $\omega = 0$ ppm and the CEST pool at $\omega \approx 50$ ppm decreases as the temperature increases, but also both peaks broaden, corresponding to an increased exchange rate [109]. From further analysis of this data, we inferred that one should wait at least 40 min to guarantee a sufficiently stable temperature once the VTU has been set (this value will vary depending on the heat capacity of the specific setup, of course). Note that recording a single CEST spectrum with comparable spectral resolution the conventional way would have taken more than half an hour, which would be clearly too long to achieve the required temporal resolution to capture the temperature build-up. To our knowledge, this experiment represented the first demonstration of monitoring a dynamic process with sub-minute resolution using CEST spectroscopy.

Moreover, we further extended UCS with the capability of measuring multiple samples simultaneously (if certain requirements on the sample geometry are satisfied, as discussed below). We achieved this by including a multi-slice loop into the original UCS sequence: After the saturation pulse is applied, instead of only one, multiple slices are excited and recorded sequentially. Since the additional readout time per slice slice (17.5 ms) is very small, this modification allows to investigate multiple samples in almost the same amount of time that the original UCS sequence would require for a single sample. We successfully demonstrated the extended UCS sequence using three samples containing different concentrations of the contrast agent EuDOTA-4AmC, cutting down the scan time from 1.5 min (original UCS) or even from 1.5 h (conventional CEST spectroscopy) to 34 s (extended UCS).

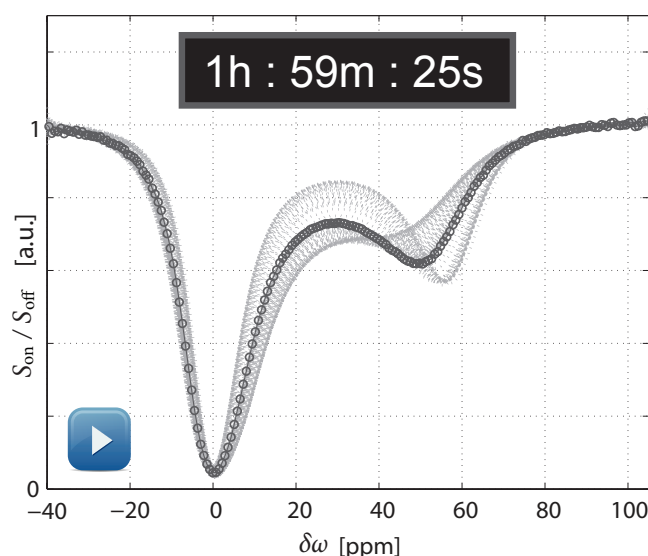


Figure 3.10.: This movie shows the ^1H CEST spectra during temperature changes, acquired with ultrafast CEST spectroscopy. In the bottom right corner, the set point of the temperature controller (VTU) is denoted. If the movie is not displayed correctly, try to open this document with Adobe Acrobat Reader.

Note that a single slice is only allowed to cover a single sample tube, otherwise one spectrum will have contributions from multiple samples. This means that for example two nested sample tubes as used in our Hyper-CEST two-compartment phantom could not be investigated with this method (however, arbitrary sample tube arrangements will become feasible with ultrafast CEST imaging, as described later in section 3.2.3).

In summary, we successfully implemented and applied an ultrafast CEST spectroscopy sequence for proton CEST contrast agents and exploited its drastically reduced acquisition time for dynamic temperature monitoring. These promising results motivated us to apply UCS to Hyper-CEST as well, as described in the following section.

3.2.2. Ultrafast Hyper-CEST spectroscopy

— corresponding to publication P4

The application of UCS to accelerate the acquisition of Hyper-CEST spectra [P4] is in principle straightforward. However, there are some differences when switching from thermally polarized protons to hyperpolarized nuclei:

1. The magnetization of dissolved xenon is in general much smaller than the proton magnetization (see box on page 51). This is not so much of a problem for conventional Hyper-CEST, where all the magnetization from one xenon delivery is available for a single spectral data point. In UCS however, the magnetization is shared among all spectral data points. Therefore, using UCS with Hyper-CEST might lead to SNR

Why is the NMR signal of hyperpolarized Xe still smaller than that of thermally polarized water?

This might seem confusing, having motivated hyperpolarized xenon MRI with an increased sensitivity compared to proton MRI. However, remember that sensitivity refers to the ability to detect small concentrations of a biochemical target, and is mainly achieved by a large average magnetization or signal *per nuclear spin*, i.e. a large polarization. Since at room temperature the mere concentration of NMR active ^{129}Xe dissolved in water ($\sim 107\ \mu\text{M}$ assuming a total xenon fraction of 2%, 3.5 bar overpressure and an Ostwald solubility of 0.11 [41]) is much lower than the concentration of protons in water ($\sim 110\ \text{M}$), the xenon magnetization per voxel is despite hyperpolarization still nearly 450 times weaker than the proton magnetization per voxel (assuming polarizations of 25% and 0.003% for xenon and protons, respectively).*

*Notably, even for the same spin concentration and polarization, the proton signal would be larger than the xenon signal. This is because upon closer inspection, the NMR signal is not only proportional to the magnitude of the magnetization, but also to the Larmor frequency [78]. Protons possess a larger gyromagnetic ratio than xenon, and hence precess at a higher Larmor frequency.

issues.

2. The hyperpolarization does not recover again once it has been used up (section 2.2.1). Therefore, after each scan, fresh hyperpolarized xenon has to be delivered to the sample (which in our setup takes about 10 - 20 s).
3. Since T_1 is relatively slow for xenon dissolved in water ($\sim 1\ \text{min}$, compared to 2.4 s for the proton CEST experiments using Eu-DOTA-4AmC and water), smashCEST can be employed to encode an entire spectrum within a single experiment.

As an initial proof of principle, we applied the UCS pulse sequence shown in Fig. 3.9A to spectral Hyper-CEST experiment using dissolved CrA as a model contrast agent. The resulting ultrafast spectrum is shown on the left side of Fig. 3.11 (blue line, acquisition time 30 s), together with a Hyper-CEST spectrum acquired the conventional way (gray line, acquisition time 10 min) for validation. The two curves match quite well, demonstrating the applicability of UCS to Hyper-CEST. However, the UCS signal was rather noisy, since the hyperpolarization has to be shared among all spectral data points, as already mentioned above. To increase SNR, we suggested to exploit the rather long T_2 of dissolved xenon (typically in the range of seconds)

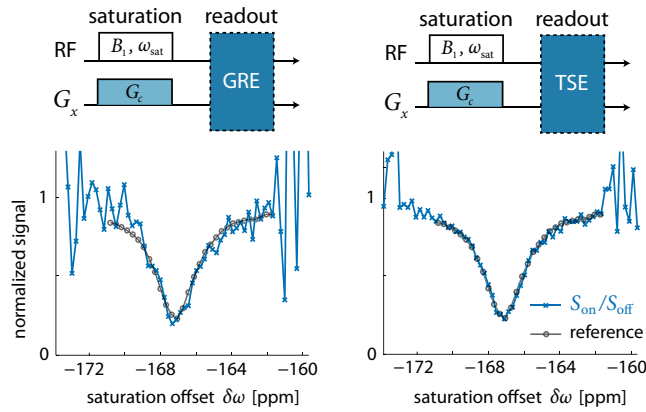


Figure 3.11: Ultrafast CEST spectroscopy (UCS) applied to hyperpolarized xenon. Left: UCS with a gradient-echo (GRE) readout as also shown in 3.9A. Right: UCS with a turbo spin-echo (TSE) readout (Fig. 2.7) without phase-encoding gradients.

with a turbo spin-echo (TSE) sequence, as already demonstrated earlier for imaging purposes (see section 3.1.1). The idea was to acquire multiple spin-echoes after the saturation preparation instead of just a single gradient-echo, and then to sum up the acquired spin-echoes to reduce the noise. The proposed UCS sequence with TSE readout is shown on the top right of Fig. 3.11 (and in more detail in [P4], Fig. 2). Below the sequence diagram, the resulting UCS spectrum is displayed (acquisition time: 31 s), exhibiting much less noise than the one acquired with the gradient-echo UCS sequence, while still showing excellent agreement with the reference CEST spectrum acquired the conventional way. We also addressed the question of how many of the acquired spin-echoes should be summed up for an optimum SNR (see [P4], Supporting Information, section 3). Here, we just give the resulting condition

$$s_{n+1} > \left(\sqrt{\frac{n+1}{n}} - 1 \right) \sum_{k=1}^n s_k \quad , \quad (3.2)$$

stating that an additional spin-echo with signal strength s_{n+1} should be included in the summation if s_{n+1} is greater than the sum over all previous n echoes weighed by the factor written in brackets.

The results shown above confirm that UCS can be conveniently applied for the detection of xenon contrast agents. The inherently reduced SNR can be partly compensated for by the application of a TSE readout.

Next, we showed that Hyper-CEST with UCS can also be combined with smashCEST, that is, with the variable flip angle approach that already allowed us to acquire Hyper-CEST MRI contrast with a single xenon delivery (see section 3.1.1). Using this approach, we demonstrated the possibility of acquiring an entire UCS Hyper-CEST spectrum after a single xenon delivery in only 15 s (see [P4], Figs. 3 and 4). Again, this might be especially useful in situations where a stable xenon redelivery cannot be guaranteed. One prerequisite for performing smashCEST UCS is a sufficiently high SNR, since the hyperpolarized magnetization has not only to be shared among all spectral

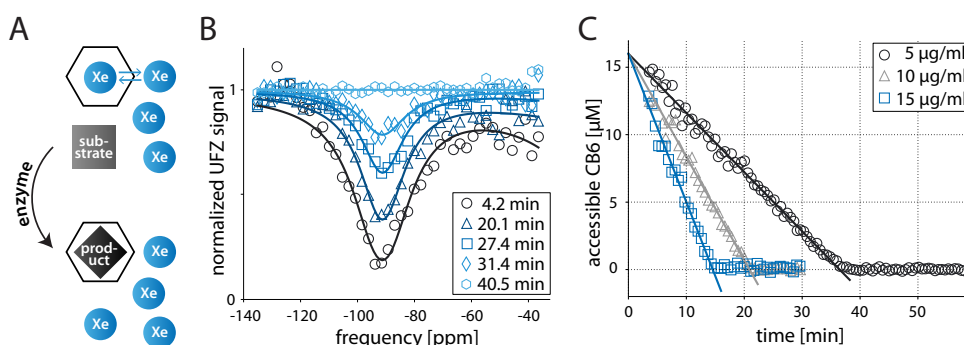


Figure 3.12.: Monitoring enzymatic activity with ultrafast Hyper-CEST spectroscopy. A: Principle of the competitive assay. B: Decreasing Hyper-CEST response with time, shown for an enzyme concentration of 5 $\mu\text{g/ml}$. C: Time curve of the concentration of accessible CB6 hosts for different enzyme concentrations. For all experiments, the substrate concentration was $[\text{Lys}] = 6 \text{ mM}$, and the host concentration was $[\text{CB6}] = 16 \text{ }\mu\text{M}$.

data points, but also among two signal acquisitions (S_{on} and S_{off}).

To summarize, the work presented in [P4] showed for the first time the application of ultrafast CEST spectroscopy to experiments using hyperpolarized xenon and demonstrated the feasibility of the detection a model contrast agent (CrA). It should be noted that similar pulse sequences have been published for ultrafast Hyper-CEST by the group of Patrick Berthault [111], however, our work was submitted first.

Application: Monitoring enzymatic activity

As an application for UCS with hyperpolarized xenon, we observed an enzymatic reaction with Hyper-CEST spectroscopy in real-time.¹ We therefore used an assay that exploits the competitive binding [112] of xenon on the one hand and the product of the enzymatic reaction (cadaverine, Cad) on the other hand to cucurbit-6-uril (CB6) host molecules, as visualized in Fig. 3.12A: Initially, only host molecules, substrate molecules (lysine, Lys), and xenon atoms are present in a buffer solution. Since xenon exchanges in and out of the host CB6, a clear response from CB6 is visible in the Hyper-CEST spectrum (spectrum at 4.2 min in Fig. 3.12B). When the enzyme (lysine decarboxylase, LDC) is added, it starts converting the substrate Lys into the product Cad. Since Cad shows a much higher binding affinity to CB6 compared to xenon, it immediately occupies the CB6 hosts and blocks them for the temporary binding of xenon. As the enzymatic reaction progresses, more and more Cad is produced, preventing more and more CB6 hosts from participating in the chemical exchange process of xenon. Therefore, the Hyper-CEST response gradually decreases with time. Finally, when

¹These results are currently still unpublished, but the preparation of a manuscript is in progress.

all CB6 molecules are occupied, the Hyper-CEST response completely vanishes (spectrum at 40.5 min in Fig. 3.12B). From the obtained series of ultrafast Hyper-CEST spectra, the concentrations of accessible CB6 can be estimated, which are in turn an indicator for the substrate concentrations and can therefore be used to display the progress of the reaction. The corresponding time curves are shown in Fig. 3.12C for three different enzyme concentrations. As expected, the substrate conversion proceeds faster at higher enzyme concentrations. From these curves, we could estimate the enzymatic activity to $79 \pm 6 \mu\text{mol min}^{-1}\text{g}^{-1}$, which agrees well with the previously measured value ($74 \mu\text{mol min}^{-1}\text{g}^{-1}$) using a fluorescence-based assay (these results are again currently still unpublished, but the preparation of a manuscript is in progress).

These experiments constitute the first dynamic monitoring of an enzymatic reaction using ultrafast Hyper-CEST spectroscopy with sub-minute resolution. Since the reactions we observed took place on a time scale of approximately 15 to 35 minutes, conventional Hyper-CEST, where the acquisition of a single spectrum takes at least 10 minutes, would have only been able to capture the start point and the end point of those reactions, but not their dynamics.

3.2.3. Ultrafast CEST imaging

— corresponding to publication P5

It was speculated in refs. [96, 111] that ultrafast CEST could be further accelerated by scanning multiple samples simultaneously using CEST imaging [113]. In section 3.2.1, we already presented an approach to investigate multiple samples at a time by exciting multiple slices. However certain restrictions on the sample tube arrangement had to be met (only one sample tube per slice), inhibiting the use of tightly packed sample tubes or nested tubes as in our Hyper-CEST bubbling phantom (Fig. 2.12). To overcome this limitation, we extended the originally purely spectroscopic method UCS with imaging capabilities, terming it ultrafast CEST imaging (UCI) [P5]. As we will see below, this method in a way combines some of the previous results of this thesis: (1) Ultrafast CEST spectroscopy using magnetic field gradients, (2) multi-slice selection and (3) sub-sampled imaging together with an image reconstruction exploiting the redundancies in the spectral domain.

The key idea for UCI is depicted in Fig. 3.13: First, a CEST gradient is applied along the longitudinal axis of the sample tubes (in this case the z -direction) to achieve spatially varying precession frequencies of the nuclear spins along that direction. While this gradient is switched on, the CEST saturation pulse is applied, just as in the case of UCS. Then, instead of acquiring the projection of the magnetization along the CEST gradient's direction, multiple slices are imaged rapidly along that direction. Thus, the spectral

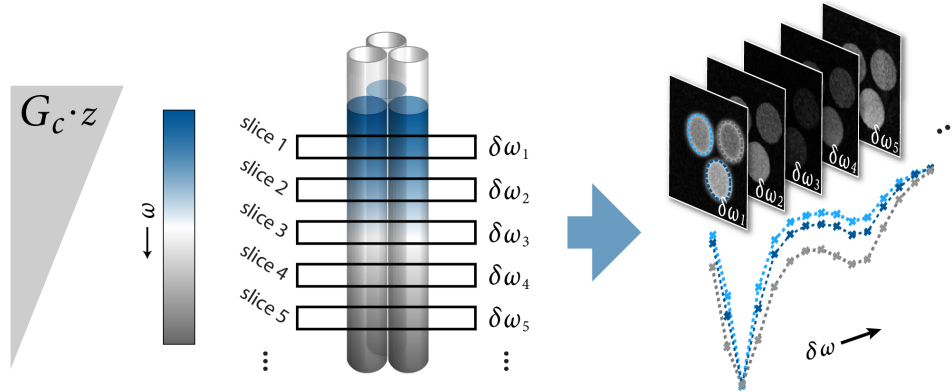


Figure 3.13.: Ultrafast CEST imaging for investigating multiple sample tubes simultaneously. The total measurement time for the CEST spectra of all three samples shown on the right side was 27 s. Using conventional CEST, the acquisition of a single spectrum would have taken more than 7 min.

dimension is resolved (each slice represents a distinct saturation frequency offset $\delta\omega_i$), while additionally the spatial information in the x - y plane is preserved. This way, all three spatial dimensions are exploited efficiently: One for encoding the saturation frequency offsets, and two for imaging. One can then recover the CEST spectra for the different samples by placing regions of interest (ROIs) in the corresponding areas in the images, and evaluating their mean pixel intensity with respect to the saturation frequency offset. Since the sample tubes can be separated due to the spatial information in the x - y plane, in principle arbitrary sample tube arrangements, such as tightly packed tubes as in ref. [113] or nested tubes become feasible.

When applied to thermally polarized water protons, one prerequisite for UCI is that the slices have to be recorded very rapidly since the saturated magnetization relaxes back to its thermal equilibrium (T_1 -relaxation, see last paragraph of section 2.3). We meet this requirement by heavily sub-sampling k -space using a radial trajectory based on a Golden Angle sampling scheme [114, 115]. We reconstructed the sub-sampled data using an iterative algorithm that exploits prior knowledge about redundancies in the image series, similar to the algorithm employed in section 3.1.2. Note that this time, sub-sampling is not used to increase the signal, but to accelerate the acquisition.

We validated the UCI sequence using three tightly packed sample tubes containing the proton CEST contrast agent Eu-DOTA-4AmC at different concentrations. CEST spectra for all three samples were acquired in only 27 s, whereas in conventional CEST, the investigation of each sample would have taken more than 7 min (see [P5], Fig. 4). The reconstruction algorithm is outlined in more detail in the Appendix of publication [P5], and furthermore a Matlab implementation is available for download (the link is given in the Supporting Information of that publication).

Note that when applied to Hyper-CEST experiments, UCI might get along without sub-sampling, since usually T_1 for dissolved xenon is much longer than for water. However, we were not yet able to apply UCI to Hyper-CEST due to SNR issues: The number of slices in UCI has to be reasonably high in order to allow for a sufficient spectral resolution (e.g. 15 slices correspond to 15 saturation frequencies). This in turn means that the slices have to be quite thin (in the experiment described above, the slice thickness was 0.45 mm, whereas we usually chose a slice thickness of 10 - 20 mm for the Hyper-CEST experiments), resulting in a xenon signal per slice that was too low to be detected within a single scan. However, in future experiments a larger xenon signal might be achieved by polarizer optimization [74, 75], using a higher xenon fraction in the gas mixture (we currently use only a fraction of 2% to 5% in our lab) and/or utilizing isotopically enriched ^{129}Xe gas.

To summarize, we extended ultrafast CEST spectroscopy with imaging capabilities, allowing for the fast acquisition of CEST spectra of multiple samples with an arbitrary sample tube arrangement.

3.2.4. Summary (for accelerated spectral encoding)

We successfully implemented and improved ultrafast CEST sequences by including multi-slice selection for the investigation of several samples and a gradient-echo readout for an improved signal-to-noise ratio. After proving its applicability for CEST experiments with thermally polarized protons (where we demonstrated dynamic temperature monitoring), we then successfully transferred the technique to Hyper-CEST, extending it with multi-echo readouts to increase the sensitivity. Besides of being useful for contrast agent screening, the gained increase in acquisition speed (about a factor of 20 for Hyper-CEST) enabled us to show for the first time dynamic monitoring of an enzymatic reaction using hyperpolarized xenon. We also combined the technique with a variable flip angle excitation (smashCEST), allowing for the acquisition of an entire Hyper-CEST spectrum with a single xenon delivery (provided that the SNR is sufficiently high): This not only further reduced measurement time (by another factor of 2), but also made the measurement robust against an unstable xenon redelivery.

Finally, we extended the described approach with imaging capabilities (ultrafast CEST imaging, UCI). This allowed us to successfully investigate three tightly packed samples of a proton CEST contrast agent within a single experiment simultaneously, which would not have been possible with previous UCS techniques. While all “ultrafast” CEST methods require a reasonably strong signal to begin with (the signal conventionally used for the acquisition of a single spectral data point is now distributed among all spectral data points), this is especially true for UCI, since here the signal is furthermore distributed among the image pixels. Although we were therefore not

yet able to apply UCI to Hyper-CEST experiments, this might become feasible through the use of enriched ^{129}Xe , a higher fraction of xenon in the gas mixture and/or future improvements regarding the hyperpolarization process.

All ultrafast methods encode spectral information along a spatial dimension, and therefore require the sample under investigation to be homogeneous at least along this dimension.² They will therefore be especially useful for *in vitro* experiments, e.g. for contrast agent screening: For instance, to assess how efficient a certain agent at a certain concentration is, and how well two different agents can be combined for multiplexing (e.g. by determining their spectral overlap). Since for these investigations a large number of experiments with different saturation pulse powers and agent concentrations are necessary (which would take hours with conventional CEST), we believe that the ultrafast methods will be very helpful for the study and the development of new (Hyper-)CEST contrast agents.

Furthermore, UCS might prove useful for the fast chemical analysis of complex mixtures targeting multiple substances with multiple molecular sensors. Next to biological samples, one could also think of analyzing environmental samples or food samples.

Additionally, ultrafast methods can be used to dynamically monitor processes in sub-minute resolution using (Hyper-)CEST spectroscopy. While we demonstrated this for the observation of temperature changes and enzymatic reactions, further processes such as pH changes [110, 116] or protein folding [117] might be observable as well.

The above discussion suggests that ultrafast CEST spectroscopy and imaging have great potential for various CEST or Hyper-CEST *in vitro* experiments, whenever a reduced acquisition time is desired and sufficient signal is available.

²However, the samples can be partly inhomogeneous (for multi-slice UCS and for UCI) to allow for the investigation of multiple samples at once.

Conclusion

The aim of this thesis was to improve the NMR detection of reversibly bound xenon from a signal encoding perspective, especially in the context of xenon biosensors. To this end, we presented the following techniques:

1. We implemented **single-shot imaging** sequences (namely, EPI and TSE) for Hyper-CEST, that efficiently exploit the available hyperpolarization, and hence allow for fast and sensitive encoding of spatial information. In particular, we showed xenon MRI of a contrast agent in the nanomolar regime in less than two minutes. This speedup enabled us to acquire for the first time entire spectral Hyper-CEST image series (e.g. for performing multiplexing) in an acceptable time frame of around 12 minutes. Using the then state-of-the-art technique, an equivalent conventional measurement would have taken almost 4 hours. Furthermore, the fast image acquisition enabled us to dynamically follow the diffusion of contrast agent molecules through a dialysis tubing. This demonstrates the feasibility of future studies monitoring the uptake of xenon biosensors, similar to dynamic contrast enhanced (DCE) measurements as routinely employed in ^1H MRI [118].
2. We increased the signal-to-noise ratio (SNR) of spectral Hyper-CEST images by exploiting pixel correlations in the spectral domain using **principal component analysis**. Identifying and removing principal components that mainly represented image noise led to an effective denoising of the data set, hence increasing SNR via a simple post-processing step. Notably, this method cannot only readily be applied to any series of spectral Hyper-CEST images, but also to conventional ^1H CEST data sets.
3. We additionally increased the SNR of spectral Hyper-CEST images by performing **sub-sampling**, i.e. we encoded less data than conventionally required by the Nyquist sampling criterion. This way, we could distribute the available hyperpolarization among less data points, effectively increasing the available signal intensity per data point. To recover reliable images from the sub-sampled data, we implemented an image reconstruction algorithm that incorporated prior knowledge

to compensate for the missing data points: Namely, the algorithm exploits exactly the same data correlations mentioned in the previous point. Sub-sampling can again also be applied to conventional ^1H CEST data sets, however in this case not yielding better SNR (since the initial thermal magnetization anyway recovers rapidly due to relaxation), but merely leading to a reduced acquisition time [119].

4. Hyper-CEST is an indirect detection technique that requires at least two scans with identical starting conditions to generate meaningful contrast: a CEST-weighted scan including the saturation preparation and a reference scan. The **smashCEST** technique allows us to encode these two scans using only a single delivery of xenon by utilizing two variable excitation flip angles (45° - 90°). Since therefore inherently identical starting conditions are established for both scans, the xenon redelivery needs no longer to be highly consistent, as it is the case for conventional Hyper-CEST. This technique is especially useful when such a consistent redelivery cannot be guaranteed, e.g. for polarizer setups without optimization for continuous flow and/or for future *in vivo* experiments. SmashCEST reduces SNR, since the signal from one xenon batch is shared among two scans, however, this is made up for by a reduced acquisition time.
5. We significantly accelerated the acquisition of both spectral ^1H CEST and Hyper-CEST *in vitro* experiments using **ultrafast CEST spectroscopy** (UCS). This is achieved by encoding the saturation frequencies along a spatial dimension using a magnetic field gradient, reducing the amount of required scans for the CEST spectrum from one per spectral data point to in total only two. Extending the method with a multi-slice loop, we demonstrated the investigation of multiple samples at the same time. We then applied the technique for monitoring dynamic processes with sub-minute resolution: We monitored temperature changes in a sample with ultrafast ^1H CEST spectroscopy, and we followed an enzymatic reaction with ultrafast Hyper-CEST spectroscopy.
6. We extended UCS with MR imaging capabilities, terming it **ultrafast CEST imaging** (UCI). Just as in UCS, a magnetic field gradient is applied to encode the saturation frequencies along a spatial dimension. Then, instead of acquiring the projection of the sample as in UCS, we used a fast multi-slice readout to obtain 2D images for slices representing different saturation frequencies. Hence, an entire spectral CEST image series could be obtained using only two scans. The additional encoding of 2D spatial information allows for the investigation of multiple sample tubes that can (as opposed to UCS) be arbitrarily arranged.

We are convinced that these techniques will contribute to pushing forward the development of new molecular sensing applications with hyperpolarized xenon. Regarding molecular imaging, the next step that remains to be done is to demonstrate xenon biosensor detection *in vivo*, e.g. in small animals. For such experiments to succeed, two aspects must be considered on the technical side: First, the xenon signal and the subsequent signal processing must enable a sufficiently high signal-to-noise ratio to allow for xenon MRI. Second, suitable biosensors or contrast agents must be available, i.e. biocompatible constructs that (1) show specific binding to a certain molecular target with high affinity, that (2) possess a host moiety that ideally encapsulates exclusively xenon atoms (such that other nearby biological molecules do not block the host moiety), and that (3) preferably show a notable xenon chemical shift difference between their target-bound and their unbound state.

With regard to the first aspect (i.e. xenon signal-to-noise), this work demonstrates the promising potential of the presented Hyper-CEST single-shot imaging techniques and our optimized polarizer setup, which have already proven useful e.g. for live cell experiments [P6, 31]. Moreover, with sub-sampled acquisition and principal component analysis we have two further techniques at hand that can improve on the signal-to-noise ratio whenever spectral Hyper-CEST image series are recorded. As the xenon *in vivo* signal after inhalation or injection has already been reported to be strong enough to allow for xenon imaging in different organs of live rodents [16, 46–48], we expect that it will also suffice for *in vivo* Hyper-CEST imaging experiments. The problem of a possibly inconsistent xenon delivery can be tackled with smashCEST, making each scan internally self-referenced. Which particular MRI pulse sequence (e.g. EPI, TSE or GRE) is best suited will in the end depend on the particular conditions encountered *in vivo* (e.g. on the relaxation times and the exchange rates).

However, as mentioned above, the success of xenon biosensing will also depend on a second aspect, i.e. the availability of suitable biosensors.¹ As none of the already existing biosensors has been tested in living organisms so far, it is likely that additional research has to be invested into developing such *in vivo* compatible sensors. In this context, fast and efficient screening methods are highly desirable to rapidly investigate potential candidate compounds. The “ultrafast” CEST techniques we proposed in this thesis will greatly facilitate these screenings, as they strongly accelerate *in vitro* CEST spectroscopy and hence strongly reduce the required measurement time.

In the following, some suggestions are listed how some of the techniques presented above could be improved, extended or applied in future research. For instance, the utility of other promising single-shot MRI sequences such as

¹This is not only true for molecular imaging *in vivo*, but also for *in vitro* chemical sensing applications.

gradient- and spin-echo (GRASE) [120] or spiral imaging [121] could be investigated in the context of Hyper-CEST. While GRASE in some sense combines the benefits of EPI (fast imaging) and TSE sequences (less artifacts), spiral trajectories have other interesting features: Since the data acquisition starts in the center of k -space, the effective echo time can be made “ultra-short” [122], leading to negligible T_2^* attenuation. Furthermore, due to the increased “incoherency” of spiral trajectories compared to Cartesian ones, spirals are often used in conjunction with sub-sampling [100, 123]. In the context of our sub-sampled Hyper-CEST experiments, an interleaved spiral sequence could be equipped with a variable excitation flip angle, just as we equipped a gradient-echo sequence with a variable excitation flip angle. This way, a higher degree of sub-sampling might be achieved, promising a further increased signal per data point. However, spiral trajectories are more sensitive to gradient imperfections and more tedious in terms of image reconstruction than Cartesian trajectories.

Another way of achieving a higher degree of sub-sampling is the incorporation of additional prior knowledge into the image reconstruction process, such as the sparsity in a known transform domain (e.g. total variation or wavelet). Imaginable is also a model based reconstruction approach similar to refs. [124, 125], where simultaneously with image recovery, also relevant parameters (i.e. relaxation times and exchange rate constants) could be extracted from the data.

Regarding image post-processing, alternative data decomposition methods used in mixture analysis such as multivariate curve resolution (MCR) [126, 127] could be employed instead of PCA. While the principal components extracted in PCA often do not have any physical meaning,² the “components” of MCR must fulfill certain user-defined physical constraints (e.g. non-negativity), such that they are often easier to interpret. The idea would be to feed an adapted MCR algorithm with spectral Hyper-CEST image data of a xenon biosensor sample. The algorithm then might not only find out the number of biosensors present in the sample (i.e. the number of significant components), but could possibly also extract denoised images of the spatial distribution of those sensors separately (i.e. the actual components).

The ultrafast CEST methods presented in this thesis might not only be useful for efficient contrast agent screening, but also more generally prove useful for the study of exchange processes in host-guest complexes (such as cucurbit- $[n]$ -urils [64, 128], cyclodextrins [129, 130] and gas-binding proteins [35, 131]) with Hyper-CEST spectroscopy. Particularly useful results could be achieved when the resulting spectra are evaluated with an appropriate quantitative theoretical model [94, 95]. Furthermore, fast methods might be interesting for the optimization of pulsed saturation schemes [132]: Here,

²They rather have an abstract, mathematical meaning, as they are obtained by maximizing the explained variance while being orthogonal to each other.

the effect of various parameters such as pulse train length, duty cycle, pulse shape and strength is often investigated. Ultrafast CEST could help to substantially reduce the acquisition time for the large number of experiments required in this context. Furthermore, ultrafast methods might be useful for the optimization of novel saturation schemes such as uniform MT[133], or of novel encoding schemes such as frequency-labeled exchange transfer (FLEX) [134], where a magnetic field gradient could be used to encode different evolution times in a single scan.

As the ultrafast CEST imaging technique presented in this thesis involves sub-sampling, it could be improved using the same techniques as discussed above, i.e. incorporation of additional prior knowledge and the use of a more “incoherent” trajectory (e.g. a spiral). Furthermore, instead of the multi-slice readout, one could also apply a 3D MRI readout, possibly enabling a more efficient acceleration with compressed sensing and parallel imaging [115, 135].

In ref. [58], Berthault et al. investigated samples in a phantom tube with multi-slice imaging to encode multiple CEST saturation times within a single experiment (for one saturation offset). Combining this idea with UCS could yield entire CEST spectra (i.e. multiple offsets) for different saturation times within a single experiment. Such data could be useful for the Laplace transform analysis of different CEST resonances [136] or for the global fitting of CEST spectra to obtain stable fitting results [95].

The techniques described in this thesis are mainly intended to improve the NMR detection of reversibly bound xenon, and they have to date been successfully applied in various research projects [29, 30, 31, 97, 98, P6]. However, most of these techniques are also of use for the field of conventional proton CEST: For instance, PCA analysis can be used to denoise spectral proton CEST images the same way we used it for Hyper-CEST images. Furthermore, the presented sub-sampling methods for Cartesian and radial sequences can likewise be employed for proton MRI, possibly leading to a reduced acquisition time [119]. Finally, as demonstrated in this thesis, the ultrafast CEST techniques are anyway applicable for both Hyper-CEST and conventional CEST.

Overall, the data encoding and post-processing techniques for (Hyper-) CEST presented in this thesis might help to extend the scope of molecular sensing with hyperpolarized xenon to further biological and chemical applications. In addition, we expect that they will prove useful in the context of future xenon biosensor studies *in vivo*.

List of publications

In the following, all publications I authored or co-authored during the course of this thesis are listed, among them four journal articles with first authorship [P2-P5] and one journal article with shared first authorship [P1]. The name(s) of the first author(s) is(are) shown underlined.

Journal articles

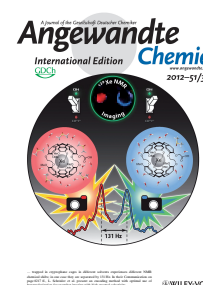
- [P1] Martin Kunth[†], Jörg Döpfert[†], Christopher Witte, Federica Rossella, Leif Schröder

Optimized Use of Reversible Binding for Fast and Selective NMR Localization of Caged Xenon

Angew. Chem. Int. Edit. **52** 8281 – 8284 (2012)

DOI: 10.1002/anie.201202481

In this communication, to which my colleague Martin Kunth and me contributed equally, we demonstrate imaging of xenon contrast agents with strongly increased sensitivity and speed while preserving spectral selectivity to detect multiple agents simultaneously. This is achieved by combining Hyper-CEST with a fast single shot read-out (EPI) that makes optimized use of the available hyperpolarization. (see section 3.1.1 on page 35). While we implemented the MRI techniques (EPI, smashCEST) and prepared the manuscript draft together, Martin Kunth performed the diffusion measurements whereas I did the spectral measurements to detect multiple different agents.



highlighted as inside cover article

[†] shared first authorship

- [P2] Jörg Döpfert, Christopher Witte, Martin Kunth, Leif Schröder
Sensitivity Enhancement of (Hyper-)CEST Image Series by Exploiting Redundancies in the Spectral Domain

Contrast Media Mol. I. **9** 100 – 107 (2014)

DOI: 10.1002/cmmi.154

This research article presents my work on further improving the quality of spectral Hyper-CEST images by exploiting correlations in the spectral domain. Two approaches are proposed: PCA based post-processing to reduce the noise and sub-Nyquist-sampling with constrained reconstruction to increase the signal per data point. I implemented the MRI sequences, performed the experiments, did the data evaluation and post-processing and prepared the manuscript draft.

- [P3] Jörg Döpfert, Christopher Witte, Leif Schröder
Slice-Selective Gradient-Encoded CEST Spectroscopy for Monitoring Dynamic Parameters and High-Throughput Sample Characterization

J. Magn. Reson. **237** 34 – 39 (2013)

DOI: 10.1016/j.jmr.2013.09.007

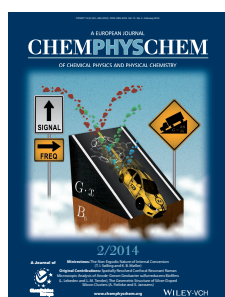
In this paper, magnetic field gradients are employed to encode the spectral CEST information instead of sweeping the saturation pulse frequency. This drastically accelerates the measurement of CEST spectra and hence allows fast screening of sample contrast agents as well as monitoring of dynamic parameters such as temperature changes. I implemented the MRI sequences, performed the experiments, did the data evaluation and post-processing and prepared the manuscript draft.

- [P4] Jörg Döpfert, Christopher Witte, Leif Schröder
Fast Gradient-Encoded CEST Spectroscopy of Hyperpolarized Xenon

ChemPhysChem **15** 261 – 264 (2014)

DOI: 10.1002/cphc.201300888

In this communication, the concept of gradient encoding the spectral CEST information as presented for ^1H nuclei in [P3] and ref. [96] is for the first time applied to hyperpolarized xenon. To increase the signal-to-noise ratio, repeated spin-echo refocusing is employed. The use of a variable flip angle furthermore allows the acquisition of entire CEST spectra with only a single xenon delivery. I implemented the MRI sequences, performed the experiments, did the data evaluation and post-processing and prepared the manuscript draft.



highlighted as
front cover article

- [P5] Jörg Döpfert, Moritz Zaiss, Christopher Witte, Leif Schröder

Ultrafast CEST Imaging

J. Magn. Reson. **243** 47 – 53 (2014)

DOI: 10.1016/j.jmr.2014.03.008

In this communication, the gradient encoding of spectral CEST information is combined with MR imaging. Fast gradient-encoded CEST images of multiple sample tubes are obtained by using a heavily sub-sampled multi-slice imaging sequence. To reconstruct the images from the sub-sampled data, again correlations in the spectral domain are exploited. This work thus represents in a way a combination of the publications [P2] and [P3]. I implemented the MRI sequences, performed the experiments, did the data evaluation and post-processing and prepared the manuscript draft.

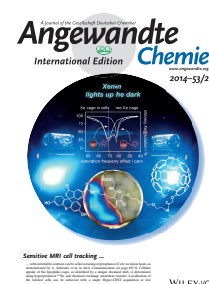
- [P6] Stefan Klippel, Jörg Döpfert, Jabadurai Jayapaul, Martin Kunth, Federica Rossella, Matthias Schnurr, Christopher Witte, Christian Freund, Leif Schröder

Cell Tracking with Caged Xenon: Using Cryptophanes as MRI Reporters upon Cellular Internalization

Angew. Chem. Int. Edit. **53** 493 – 496 (2014)

DOI: 10.1002/anie.201307290

In this work, we demonstrate the first live cell tracking with MRI using xenon contrast agents. I implemented the employed single-shot imaging sequences, helped with the MRI acquisition and wrote the scripts for image processing and data evaluation.



highlighted as
back cover article

Conference contributions

- [C1] Jörg Döpfert, Martin Kunth, Christopher Witte, Federica Rossella, Leif Schröder

Fast and Selective MRI of Xenon Biosensors

Spring Meeting of the Deutsche Physikalische Gesellschaft (DPG), Berlin (2012)

- [C4] Jörg Döpfert, Martin Kunth

Schnelle und Selektive NMR-Spektroskopische Lokalisierung von Eingeschlossenem Xenon durch Optimales Einbeziehen der Reversiblen Bindung

Annual Meeting of the German Chapter of the International Society for Magnetic Resonance in Medicine, Ulm (2012)

- [C3] Jörg Döpfert, Christopher Witte, Martin Kunth, Michael Beyer-
mann, Leif Schröder
**Improved Evaluation of (Hyper-)CEST Images Using the Spectral
Dimension**
*Annual Meeting of the International Society for Magnetic Resonance
in Medicine* p.1667, Melbourne, Australia (2012)
- [C2] Jörg Döpfert, Christopher Witte, Martin Kunth, Leif Schröder
**Sub-Sampling for Improved Use of Magnetization in Spectral
Hyper-CEST Image Series**
Experimental Nuclear Magnetic Resonance Conference (ENC) Asilo-
mar, USA (2013)
- [C5] Jörg Döpfert, Moritz Zaiss, Christopher Witte, Leif Schröder
Ultrafast CEST Imaging
World Molecular Imaging Congress Seoul, Korea (2014)

Bibliography

- [1] M. L. James and S. S. Gambhir: A molecular imaging primer: Modalities, imaging agents, and applications *Physiol. Rev.* **92** 897–965 (2012). Cited on pages 1, 4, 8 and 36
- [2] W. C. W. Chan and S. Nie: Quantum dot bioconjugates for ultrasensitive nonisotopic detection *Science* **281** 2016–2018 (1998). Cited on page 1
- [3] K. B. Mogensen, H. Klank and J. P. Kutter: Recent developments in detection for microfluidic systems *Electrophoresis* **25** 3498–3512 (2004). Cited on page 1
- [4] B. Driehuys: Toward molecular imaging with xenon MRI *Science* **314** 432–433 (2006). Cited on pages 1 and 6
- [5] L. Schröder: Xenon for NMR biosensing – inert but alert *Phys. Medica* **29** 3–16 (2011). Cited on pages 1, 3, 10 and 25
- [6] R. N. Bryan: Introduction to the Science of Medical Imaging *Cambridge University Press* (2009). Cited on page 1
- [7] K. W.-Y. Chan and W.-T. Wong: Small molecular gadolinium(III) complexes as MRI contrast agents for diagnostic imaging *Coord. Chem. Rev.* **251** 2428 – 2451 (2007). Cited on page 1
- [8] C. Sun, O. Veiseh, J. Gunn, C. Fang, S. Hansen, D. Lee, R. Sze, R. G. Ellenbogen, J. Olson and M. Zhang: In vivo MRI detection of gliomas by chlorotoxin-conjugated superparamagnetic nanoprobe *Small* **4** 372–379 (2008). Cited on page 1
- [9] I. Hancu, W. T. Dixon, M. Woods, E. Vinogradov, A. D. Sherry and R. E. Lenkinski: CEST and PARACEST MR contrast agents *Acta Radiol.* **51** 910–923 (2010). Cited on page 1
- [10] C. Witte and L. Schröder: NMR of hyperpolarised probes *NMR Biomed.* **26** 788–802 (2013). Cited on pages 1 and 25
- [11] B. M. Goodson: Nuclear magnetic resonance of laser-polarized noble gases in molecules, materials, and organisms *J. Magn. Reson.* **155** 157 – 216 (2002). Cited on page 1

- [12] M. S. Albert, G. D. Cates, B. Driehuys, W. Happer, B. Saam, C. S. Springer and A. Wishnia: Biological magnetic resonance imaging using laser-polarized ^{129}Xe *Nature* **370** 199–201 (1994). Cited on page 2
- [13] K. Ruppert, J. R. Brookeman, K. D. Hagspiel and J. P. Mugler: Probing lung physiology with xenon polarization transfer contrast (XTC) *Magn. Reson. Med.* **44** 349–357 (2000). Cited on page 2
- [14] B. Driehuys, G. P. Cofer, J. Pollaro, J. B. Mackel, L. W. Hedlund and G. A. Johnson: Imaging alveolar–capillary gas transfer using hyperpolarized ^{129}Xe MRI *Proc. Natl. Acad. Sci.* **103** 18278–18283 (2006). Cited on page 2
- [15] B. Driehuys, J. Pollaro and G. P. Cofer: In vivo MRI using real-time production of hyperpolarized ^{129}Xe *Magn. Reson. Med.* **60** 14–20 (2008). Cited on page 2
- [16] M. L. Mazzanti, R. P. Walvick, X. Zhou, Y. Sun, N. Shah, J. Mansour, J. Gereige and M. S. Albert: Distribution of hyperpolarized xenon in the brain following sensory stimulation: Preliminary MRI findings *PLoS ONE* **6** e21607 (2011). Cited on pages 2, 7, 9 and 61
- [17] J. P. Mugler, B. Driehuys, J. R. Brookeman, G. D. Cates, S. S. Berr, R. G. Bryant, T. M. Daniel, E. E. De Lange, J. H. Downs, C. J. Erickson et al.: MR imaging and spectroscopy using hyperpolarized ^{129}Xe gas: Preliminary human results *Magn. Reson. Med.* **37** 809–815 (1997). Cited on page 2
- [18] M. Kirby and G. Parraga: Pulmonary functional imaging using hyperpolarized noble gas MRI: Six years of start-up experience at a single site *Acad. Radiol.* **20** 1344–1356 (2013). Cited on page 2
- [19] J. P. Mugler and T. A. Altes: Hyperpolarized ^{129}Xe MRI of the human lung *J. Magn. Reson. Imag.* **37** 313–331 (2013). Cited on page 2
- [20] Y. V. Chang, J. D. Quirk, I. C. Ruset, J. J. Atkinson, F. W. Hersman and J. C. Woods: Quantification of human lung structure and physiology using hyperpolarized ^{129}Xe *Magn. Reson. Med.* **71** 339–344 (2014). Cited on page 2
- [21] K. Qing, J. P. Mugler, T. A. Altes, Y. Jiang, J. F. Mata, G. W. Miller, I. C. Ruset, F. W. Hersman and K. Ruppert: Assessment of lung function in asthma and COPD using hyperpolarized ^{129}Xe chemical shift saturation recovery spectroscopy and dissolved-phase MRI *NMR Biomed.* **27** 1490–1501 (2014). Cited on page 2

- [22] K. K. Palaniappan, M. B. Francis, A. Pines and D. E. Wemmer: Molecular sensing using hyperpolarized xenon NMR spectroscopy *Isr. J. Chem.* **54** 104–112 (2014). Cited on pages 2 and 17
- [23] M. M. Spence, S. M. Rubin, I. E. Dimitrov, E. J. Ruiz, D. E. Wemmer, A. Pines, S. Q. Yao, F. Tian and P. G. Schultz: Functionalized xenon as a biosensor *Proc. Natl. Acad. Sci.* **98** 10654–10657 (2001). Cited on pages 2, 6 and 8
- [24] L. Schröder, T. J. Lowery, C. Hilty, D. E. Wemmer and A. Pines: Molecular imaging using a targeted magnetic resonance hyperpolarized biosensor *Science* **314** 446–449 (2006). Cited on pages 3, 28, 33, 35 and 36
- [25] Y. Bai, P. A. Hill and I. J. Dmochowski: Utilizing a water-soluble cryptophane with fast xenon exchange rates for picomolar sensitivity NMR measurements *Anal. Chem.* **84** 9935–9941 (2012). Cited on pages 3 and 43
- [26] T. K. Stevens, R. M. Ramirez and A. Pines: Nanoemulsion contrast agents with sub-picomolar sensitivity for xenon NMR *J. Am. Chem. Soc.* **135** 9576–9579 (2013). Cited on pages 3 and 10
- [27] K. K. Palaniappan, R. M. Ramirez, V. S. Bajaj, D. E. Wemmer, A. Pines and M. B. Francis: Molecular imaging of cancer cells using a bacteriophage-based ^{129}Xe NMR biosensor *Angew. Chem. Int. Edit.* **52** 4849–4853 (2013). Cited on pages 3, 9 and 10
- [28] P. Berthault, G. Huber and H. Desvaux: Biosensing using laser-polarized xenon NMR/MRI *Prog. Nucl. Mag. Res. Sp.* **55** 35–60 (2009). Cited on pages 3, 9, 26, 35 and 43
- [29] M. Schnurr, K. Sydow, H. M. Rose, M. Dathe and L. Schröder: Brain endothelial cell targeting via a peptide-functionalized liposomal carrier for xenon Hyper-CEST MRI *Adv. Healthcare Mater.* **4** 40–45 (2014). Cited on pages 3, 9, 33, 37, 43 and 63
- [30] H. M. Rose, C. Witte, F. Rossella, S. Klippel, C. Freund and L. Schröder: Development of an antibody-based, modular biosensor for ^{129}Xe NMR molecular imaging of cells at nanomolar concentrations *Proc. Natl. Acad. Sci.* **111** 11697–11702 (2014). Cited on pages 3, 8, 9, 33, 37, 43 and 63
- [31] S. Klippel, C. Freund and L. Schröder: Multichannel MRI labeling of mammalian cells by switchable nanocarriers for hyperpolarized xenon *Nano Lett.* **14** 5721–5726 (2014). Cited on pages 3, 17, 37, 43, 61 and 63
- [32] D. E. Sosnovik and R. Weissleder: Emerging concepts in molecular MRI *Curr. Opin. Chem. Biol.* **18** 4–10 (2007). Cited on page 4

- [33] P. C. M. Zijl and N. N. Yadav: Chemical exchange saturation transfer (CEST): what is in a name and what isn't? *Magn. Reson. Med.* **65** 927–948 (2011). Cited on pages 6, 28 and 31
- [34] P. Berthault, A. Bogaert-Buchmann, H. Desvaux, G. Huber and Y. Boulard: Sensitivity and multiplexing capabilities of MRI based on polarized ^{129}Xe biosensors *J. Am. Chem. Soc.* **130** 16456–16457 (2008). Cited on pages 6 and 10
- [35] M. G. Shapiro, M. Ramirez, L. Sperling, G. Sun, J. Sun, A. Pines, D. Schaffer and V. S. Bajaj: Genetically encoded reporters for hyperpolarized xenon magnetic resonance imaging *Nat. Chem.* **6** 629–634 (2014). Cited on pages 6, 9, 37 and 62
- [36] P. D. Garimella, T. Meldrum, L. S. Witus, M. Smith, V. S. Bajaj, D. E. Wemmer, M. B. Francis and A. Pines: Hyperpolarized xenon-based molecular sensors for label-free detection of analytes *J. Am. Chem. Soc.* **136** 164–168 (2014). Cited on page 6
- [37] M. Gatzke, G. Cates, B. Driehuys, D. Fox, W. Happer and B. Saam: Extraordinarily slow nuclear spin relaxation in frozen laser-polarized ^{129}Xe *Phys. Rev. Lett.* **70** 690–693 (1993). Cited on page 6
- [38] A.-M. Oros and N. J. Shah: Hyperpolarized xenon in NMR and MRI *Phys. Med. Biol.* **49** R105 (2004). Cited on pages 6, 8 and 17
- [39] B. Chann, I. Nelson, L. Anderson, B. Driehuys and T. Walker: ^{129}Xe -Xe molecular spin relaxation *Phys. Rev. Lett.* **88** 113201 (2002). Cited on page 6
- [40] A. K. Venkatesh, L. Zhao, D. Balamore, F. A. Jolesz and M. S. Albert: Evaluation of carrier agents for hyperpolarized xenon MRI *NMR Biomed.* **13** 245–252 (2000). Cited on page 6
- [41] A. Cherubini and A. Bifone: Hyperpolarised xenon in biology *Prog. Nucl. Mag. Res. Sp.* **42** 1–30 (2003). Cited on pages 6 and 51
- [42] M. S. Albert, D. F. Kacher, D. Balamore, A. K. Venkatesh and F. A. Jolesz: T_1 of ^{129}Xe in blood and the role of oxygenation *J. Magn. Reson.* **140** 264–273 (1999). Cited on pages 6 and 7
- [43] J. Wolber, A. Cherubini, A. S. K. Dzik-Jurasz, M. O. Leach and A. Bifone: Spin-lattice relaxation of laser-polarized xenon in human blood *Proc. Natl. Acad. Sci.* **96** 3664–3669 (1999). Cited on page 7

- [44] X. Zhou, M. L. Mazzanti, J. J. Chen, Y.-S. Tzeng, J. K. Mansour, J. D. Gereige, A. K. Venkatesh, Y. Sun, R. V. Mulkern and M. S. Albert: Reinvestigating hyperpolarized ^{129}Xe longitudinal relaxation time in the rat brain with noise considerations *NMR Biomed.* **21** 217–225 (2008). Cited on pages 7 and 9
- [45] G. Norquay, G. Leung, N. J. Stewart, G. M. Tozer, J. Wolber and J. M. Wild: Relaxation and exchange dynamics of hyperpolarized ^{129}Xe in human blood *Magn. Reson. Med.* ahead of print (2014). Cited on page 7
- [46] S. D. Swanson, M. S. Rosen, K. P. Coulter, R. C. Welsh and T. E. Chupp: Distribution and dynamics of laser-polarized ^{129}Xe magnetization in vivo *Magn. Reson. Med.* **42** 1137–1145 (1999). Cited on pages 7 and 61
- [47] G. Duhamel, P. Choquet, E. Grillon, L. Lamalle, J.-L. Leviel, A. Ziegler and A. Constantinesco: Xenon-129 MR imaging and spectroscopy of rat brain using arterial delivery of hyperpolarized xenon in a lipid emulsion *Magn. Reson. Med.* **46** 208–212 (2001). Cited on pages 7, 10 and 61
- [48] X. Zhou, Y. Sun, M. Mazzanti, N. Henninger, J. Mansour, M. Fisher and M. Albert: MRI of stroke using hyperpolarized ^{129}Xe *NMR Biomed.* **24** 170–175 (2011). Cited on pages 7, 9 and 61
- [49] J. P. Mugler, B. Driehuys, J. R. Brookeman, G. D. Cates, S. S. Berr, R. G. Bryant, T. M. Daniel, E. E. De Lange, J. H. Downs, C. J. Erickson et al.: MR imaging and spectroscopy using hyperpolarized ^{129}Xe gas: Preliminary human results *Magn. Reson. Med.* **37** 809–815 (1997). Cited on page 7
- [50] W. Kilian, F. Seifert and H. Rinneberg: Dynamic NMR spectroscopy of hyperpolarized ^{129}Xe in human brain analyzed by an uptake model *Magn. Reson. Med.* **51** 843–847 (2004). Cited on page 7
- [51] F. A. Gallagher, S. E. Bohndiek, M. I. Kettunen, D. Y. Lewis, D. Soloviev and K. M. Brindle: Hyperpolarized ^{13}C MRI and PET: In vivo tumor biochemistry *J. Nucl. Med.* **52** 1333–1336 (2011). Cited on page 8
- [52] A. Schlundt, W. Kilian, M. Beyermann, J. Sticht, S. Günther, S. Höpner, K. Falk, O. Roetzschke, L. Mitschang and C. Freund: A xenon-129 biosensor for monitoring MHC–peptide interactions *Angew. Chem. Int. Edit.* **48** 4142–4145 (2009). Cited on page 8
- [53] Q. Wei, G. K. Seward, P. A. Hill, B. Patton, I. E. Dimitrov, N. N. Kuzma and I. J. Dmochowski: Designing ^{129}Xe NMR biosensors for matrix metalloproteinase detection *J. Am. Chem. Soc.* **128** 13274–13283 (2006). Cited on page 8

- [54] J. M. Chambers, P. A. Hill, J. A. Aaron, Z. Han, D. W. Christianson, N. N. Kuzma and I. J. Dmochowski: Cryptophane xenon-129 nuclear magnetic resonance biosensors targeting human carbonic anhydrase *J. Am. Chem. Soc.* **131** 563–569 (2009). Cited on page 8
- [55] V. Roy, T. Brotin, J.-P. Dutasta, M.-H. Charles, T. Delair, F. Mallet, G. Huber, H. Desvaux, Y. Boulard and P. Berthault: A cryptophane biosensor for the detection of specific nucleotide targets through xenon NMR spectroscopy *ChemPhysChem* **8** 2082–2085 (2007). Cited on page 8
- [56] N. Kotera, N. Tassali, E. Lce, C. Boutin, P. Berthault, T. Brotin, J.-P. Dutasta, L. Delacour, T. Traor.-A. Buisson, F. Taran, S. Coudert and B. Rousseau: A sensitive zinc-activated ^{129}Xe MRI probe *Angew. Chem. Int. Edit.* **51** 4100–4103 (2012). Cited on page 8
- [57] J. Zhang, W. Jiang, Q. Luo, X. Zhang, Q. Guo, M. Liu and X. Zhou: Rational design of hyperpolarized xenon NMR molecular sensor for the selective and sensitive determination of zinc ions *Talanta* **122** 101–105 (2014). Cited on page 8
- [58] N. Tassali, N. Kotera, C. Boutin, E. Leonce, Y. Boulard, B. Rousseau, E. Dubost, F. Taran, T. Brotin, J.-P. Dutasta and P. Berthault: Smart detection of toxic metal ions, Pb^{2+} and Cd^{2+} , using a ^{129}Xe NMR-based sensor *Anal. Chem.* **86** 1783–1788 (2014). Cited on pages 8, 43 and 63
- [59] G. K. Seward, Q. Wei and I. J. Dmochowski: Peptide-mediated cellular uptake of cryptophane *Bioconjug. Chem.* **19** 2129–2135 (2008). Cited on page 9
- [60] G. K. Seward, Y. Bai, N. S. Khan and I. J. Dmochowski: Cell-compatible integrin-targeted cryptophane- ^{129}Xe NMR biosensors *Chem. Sci.* **2** 1103–1110 (2011). Cited on page 9
- [61] C. Boutin, A. Stopin, F. Lenda, T. Brotin, J.-P. Dutasta, N. Jamin, A. Sanson, Y. Boulard, F. Leteurtre, G. Huber et al.: Cell uptake of a biosensor detected by hyperpolarized ^{129}Xe NMR: the transferrin case *Bioorgan. Med. Chem.* **19** 4135–4143 (2011). Cited on page 9
- [62] N. S. Khan, B. A. Riggle, G. Seward, Y. Bai and I. J. Dmochowski: A cryptophane-folate biosensor for ^{129}Xe NMR *Bioconjug. Chem.* **26** 101–109 (2014). Cited on page 9
- [63] I. R. Kleckner and M. P. Foster: An introduction to NMR-based approaches for measuring protein dynamics *BBA. - Proteins Protenom.* **1814** 942–968 (2011). Cited on page 9

- [64] G. Huber, F.-X. Legrand, V. Lewin, D. Baumann, M.-P. Heck and P. Berthault: Interaction of xenon with cucurbit[5]uril in water *ChemPhysChem* **12** 1053–1055 (2011). Cited on pages 9 and 62
- [65] B. S. Kim, Y. H. Ko, Y. Kim, H. J. Lee, N. Selvapalam, H. C. Lee and K. Kim: Water soluble cucurbit[6]uril derivative as a potential Xe carrier for ^{129}Xe NMR-based biosensors *Chem. Commun.* 2756–2758 (2008). Cited on pages 9 and 17
- [66] T. Brotin and J.-P. Dutasta: Cryptophanes and their complexes – present and future *Chem. Rev.* **109** 88–130 (2009). Cited on page 9
- [67] G. Huber, T. Brotin, L. Dubois, H. Desvaux, J.-P. Dutasta and P. Berthault: Water soluble cryptophanes showing unprecedented affinity for xenon: candidates as NMR-based biosensors *J. Am. Chem. Soc.* **128** 6239–6246 (2006). Cited on page 10
- [68] S. Mecozzi and J. Rebek: The 55% solution: A formula for molecular recognition in the liquid state *Chem. Eur. J.* **4** 1016–1022 (1998). Cited on page 10
- [69] M. M. Spence, E. J. Ruiz, S. M. Rubin, T. J. Lowery, N. Winssinger, P. G. Schultz, D. E. Wemmer and A. Pines: Development of a functionalized xenon biosensor *J. Am. Chem. Soc.* **126** 15287–15294 (2004). Cited on page 10
- [70] S. D. Swanson, M. S. Rosen, B. W. Agranoff, K. P. Coulter, R. C. Welsh and T. E. Chupp: Brain MRI with laser-polarized ^{129}Xe *Magn. Reson. Med.* **38** 695–698 (1997). Cited on page 9
- [71] B. M. Goodson: Using injectable carriers of laser-polarized noble gases for enhancing NMR and MRI *Concept. Magnetic Res.* **11** 203–223 (1999). Cited on page 10
- [72] G. Duhamel, P. Choquet, J.-L. Leviel, J. Steibel, L. Lamalle, C. Julien, F. Kober, E. Grillon, J. Derouard, M. Decorps, A. Ziegler and A. Constantinesco: In vivo ^{129}Xe NMR in rat brain during intra-arterial injection of hyperpolarized ^{129}Xe dissolved in a lipid emulsion *C. R. Seances Acad. Sci. III* **323** 529–536 (2000). Cited on page 10
- [73] H. E. Möller, M. S. Chawla, X. J. Chen, B. Driehuys, L. W. Hedlund, C. T. Wheeler and G. A. Johnson: Magnetic resonance angiography with hyperpolarized ^{129}Xe dissolved in a lipid emulsion *Magn. Reson. Med.* **41** 1058–1064 (1999). Cited on page 10

- [74] F. W. Hersman, I. C. Ruset, S. Ketel, I. Muradian, S. D. Covrig, J. Distelbrink, W. Porter, D. Watt, J. Ketel, J. Brackett, A. Hope and S. Patz: Large production system for hyperpolarized ^{129}Xe for human lung imaging studies *Acad. Radio.* **15** 683–692 (2008). Cited on pages 10, 26 and 56
- [75] P. Nikolaou, A. M. Coffey, L. L. Walkup, B. M. Gust, N. Whiting, H. Newton, S. Barcus, I. Muradyan, M. Dabaghyan, G. D. Moroz et al.: Near-unity nuclear polarization with an open-source ^{129}Xe hyperpolarizer for NMR and MRI *Proc. Natl. Acad. Sci.* **110** 14150–14155 (2013). Cited on pages 10 and 56
- [76] T. Meldrum, K. L. Seim, V. S. Bajaj, K. K. Palaniappan, W. Wu, M. B. Francis, D. E. Wemmer and A. Pines: A xenon-based molecular sensor assembled on an MS2 viral capsid scaffold *J. Am. Chem. Soc.* **132** 5936–5937 (2010). Cited on page 10
- [77] T. K. Stevens, K. K. Palaniappan, R. M. Ramirez, M. B. Francis, D. E. Wemmer and A. Pines: HyperCEST detection of a ^{129}Xe -based contrast agent composed of cryptophane-A molecular cages on a bacteriophage scaffold *Magn. Reson. Med.* **69** 1245–1252 (2013). Cited on page 10
- [78] M. E. Haacke, R. W. Brown, M. R. Thompson and R. Venkatesan: Magnetic Resonance Imaging: Physical Principles and Sequence Design *Wiley-Liss* (1999). Cited on pages 13, 15, 16 and 51
- [79] M. A. Bernstein, K. F. King and X. J. Zhou: Handbook of MRI Pulse Sequences *Elsevier Academic Press* (2004). Cited on page 13
- [80] R. A. Graaf: In Vivo NMR Spectroscopy: Principles and Techniques *Wiley* (2008). Cited on pages 13 and 14
- [81] C. P. Slichter: Principles of Magnetic Resonance *Springer-Verlag* (1989). Cited on page 13
- [82] F. Bloch: Nuclear induction *Phys. Rev.* **70** 460 (1946). Cited on page 14
- [83] K. W. Miller, N. V. Reo, A. J. Schoot Uiterkamp, D. P. Stengle, T. R. Stengle and K. L. Williamson: Xenon NMR: chemical shifts of a general anesthetic in common solvents, proteins, and membranes. *Proc. Natl. Acad. Sci.* **78** 4946–4949 (1981). Cited on page 17
- [84] P. C. Lauterbur: Image formation by induced local interactions: Examples employing nuclear magnetic resonance *Nature* **242** 190–191 (1973). Cited on page 18
- [85] T. G. Walker and W. Happer: Spin-exchange optical pumping of noble-gas nuclei *Rev. Mod. Phys.* **69** 629–642 (1997). Cited on pages 25 and 26

- [86] B. M. Goodson: Nuclear magnetic resonance of laser-polarized noble gases in molecules, materials, and organisms *J. Magn. Reson.* **155** 157–216 (2002). Cited on page 25
- [87] C. Witte, M. Kunth, F. Rossella and L. Schröder: Observing and preventing rubidium runaway in a direct-infusion xenon-spin hyperpolarizer optimized for high-resolution Hyper-CEST (chemical exchange saturation transfer using hyperpolarized nuclei) NMR *J. Chem. Phys.* **140** 084203 (2014). Cited on pages 26 and 43
- [88] H. E. Möller, X. J. Chen, B. Saam, K. D. Hagspiel, G. A. Johnson, T. A. Altes, E. E. Lange and H.-U. Kauczor: MRI of the lungs using hyperpolarized noble gases *Magn. Reson. Med.* **47** 1029–1051 (2002). Cited on page 26
- [89] L. Zhao, R. Mulkern, C.-H. Tseng, D. Williamson, S. Patz, R. Kraft, R. L. Walsworth, F. A. Jolesz and M. S. Albert: Gradient-echo imaging considerations for hyperpolarized ^{129}Xe MR *J. Magn. Reson. Ser. B* **113** 179–183 (1996). Cited on pages 26, 41 and 43
- [90] C. Hilty, T. J. Lowery, D. E. Wemmer and A. Pines: Spectrally resolved magnetic resonance imaging of a xenon biosensor *Angew. Chem. Int. Edit.* **45** 70–73 (2006). Cited on pages 27 and 44
- [91] H. M. McConnell: Reaction rates by nuclear magnetic resonance *J. Chem. Phys.* **28** 430 (1958). Cited on page 30
- [92] D. E. Woessner, S. Zhang, M. E. Merritt and A. D. Sherry: Numerical solution of the bloch equations provides insights into the optimum design of PARACEST agents for MRI *Magn. Reson. Med.* **53** 790–799 (2005). Cited on pages 30 and 31
- [93] K. Murase and N. Tanki: Numerical solutions to the time-dependent bloch equations revisited *Magn. Reson. Imaging* **29** 126–131 (2011). Cited on page 31
- [94] M. Zaiss, M. Schnurr and P. Bachert: Analytical solution for the depolarization of hyperpolarized nuclei by chemical exchange saturation transfer between free and encapsulated xenon (HyperCEST) *J. Chem. Phys.* **136** 144106 (2012). Cited on pages 31 and 62
- [95] M. Kunth, C. Witte and L. Schröder: Quantitative chemical exchange saturation transfer with hyperpolarized nuclei (qHyper-CEST): Sensing xenon-host exchange dynamics and binding affinities by NMR *J. Chem. Phys.* **141** 194202 (2014). Cited on pages 31, 62 and 63

- [96] X. Xu, J.-S. Lee and A. Jerschow: Ultrafast scanning of exchangeable sites by NMR spectroscopy *Angew. Chem. Int. Edit.* **52** (2013). Cited on pages 34, 45, 46, 47, 48, 54 and 66
- [97] R. Tyagi, C. Witte, R. Haag and L. Schröder: Dendronized cryptophanes as water-soluble xenon hosts for ^{129}Xe magnetic resonance imaging *Org. Lett.* **16** 4436–4439 (2014). Cited on pages 37, 40, 43 and 63
- [98] C. Witte, V. Martos, H. M. Rose, S. Reinke, S. Klippel, L. Schröder and C. P. R. Hackenberger: Live-cell MRI of xenon Hyper-CEST biosensors targeted to metabolically-labeled cell-surface glycans *Angew. Chem. Int. Edit.* accepted manuscript, DOI: 10.1002/anie.201410573R1 (2015). Cited on pages 37, 43 and 63
- [99] I. Jolliffe: Principal Component Analysis *Springer, New York* (2002). Cited on page 38
- [100] M. Lustig, D. Donoho and J. M. Pauly: Sparse MRI: the application of compressed sensing for rapid MR imaging *Magn. Reson. Med.* **58** 1182–1195 (2007). Cited on pages 40, 42 and 62
- [101] J.-F. Cai, E. J. Candès and Z. Shen: A singular value thresholding algorithm for matrix completion *SIAM J. Optimiz.* **20** 1956–1982 (2010). Cited on pages 41 and 42
- [102] E. Candès and B. Recht: Exact matrix completion via convex optimization *Found. Comput. Math.* **9** 717–772 (2009). Cited on page 42
- [103] M. Schnurr, C. Witte and L. Schröder: Functionalized ^{129}Xe as a potential biosensor for membrane fluidity *Phys. Chem. Chem. Phys.* **15** 14178–14181 (2013). Cited on page 43
- [104] F. Rossella, H. M. Rose, C. Witte, J. Jayapaul and L. Schröder: Design and characterization of two bifunctional cryptophane-A based host molecules for xenon magnetic resonance imaging applications *ChemPlusChem* **79** 1463–1471 (2014). Cited on page 43
- [105] S. D. Swanson: Broadband excitation and detection of cross-relaxation NMR spectra *J. Magn. Reson.* **95** 615–618 (1991). Cited on page 47
- [106] P. Callaghan: Principles of Nuclear Magnetic Resonance Microscopy *Oxford University Press, USA* (1993). Cited on page 48
- [107] S. K. Hekmatyar, R. M. Kerkhoff, S. K. Pakin, P. Hopewell and N. Bansal: Noninvasive thermometry using hyperfine-shifted MR signals from paramagnetic lanthanide complexes *Int. J. Hyperther.* **21** 561–574 (2005). Cited on page 48

- [108] S. Zhang, C. R. Malloy and A. D. Sherry: MRI thermometry based on PARACEST agents *J. Am. Chem. Soc.* **127** 17572–17573 (2005). Cited on page 48
- [109] A. X. Li, F. Wojciechowski, M. Suchy, C. K. Jones, R. H. Hudson, R. S. Menon and R. Bartha: A sensitive PARACEST contrast agent for temperature MRI: Eu³⁺-DOTAM-glycine (gly)-phenylalanine (phe) *Magn. Reson. Med.* **59** 374–381 (2008). Cited on pages 48 and 49
- [110] N. McVicar, A. X. Li, M. Such, R. H. E. Hudson, R. S. Menon and R. Bartha: Simultaneous in vivo pH and temperature mapping using a PARACEST-MRI contrast agent *Magn. Reson. Med.* **70** 1016–1025 (2012). Cited on pages 48 and 57
- [111] C. Boutin, E. Lce, T. Brotin, A. Jerschow and P. Berthault: Ultrafast z-spectroscopy for ¹²⁹Xe NMR-based sensors *J. Phys. Chem. Lett.* **4** 4172–4176 (2013). Cited on pages 53 and 54
- [112] R. N. Dsouza, A. Hennig and W. M. Nau: Supramolecular tandem enzyme assays *Chem. Eur. J.* **18** 3444–3459 (2012). Cited on page 53
- [113] G. Liu, A. A. Gilad, J. W. M. Bulte, P. C. M. Zijl and M. T. McMahon: High-throughput screening of chemical exchange saturation transfer MR contrast agents *Contrast Media Mol. I.* **5** 162–170 (2010). Cited on pages 54 and 55
- [114] S. Winkelmann, T. Schaeffter, T. Koehler, H. Eggers and O. Doessel: An optimal radial profile order based on the golden ratio for time-resolved MRI *IEEE Trans. Med. Imag* **26** 68–76 (2007). Cited on page 55
- [115] L. Feng, R. Grimm, K. T. Block, H. Chandarana, S. Kim, J. Xu, L. Axel, D. K. Sodickson and R. Otazo: Golden-angle radial sparse parallel MRI: Combination of compressed sensing, parallel imaging, and golden-angle radial sampling for fast and flexible dynamic volumetric MRI *Magn. Reson. Med.* **72** 707–717 (2013). Cited on pages 55 and 63
- [116] V. R. Sheth, G. Liu, Y. Li and M. D. Pagel: Improved pH measurements with a single PARACEST MRI contrast agent *Contrast Media Mol. I.* **7** 26–34 (2012). Cited on page 57
- [117] M. Zaiss, P. Kunz, S. Goerke, A. Radbruch and P. Bachert: MR imaging of protein folding in vitro employing nuclear-overhauser-mediated saturation transfer *NMR Biomed.* **26** 1815–1822 (2013). Cited on page 57
- [118] P. S. Tofts, G. Brix, D. L. Buckley, J. L. Evelhoch, E. Henderson, M. V. Knopp, H. B. Larsson, T.-Y. Lee, N. A. Mayr, G. J. Parker, R. E. Port, J.

- Taylor and R. M. Weisskoff: Estimating kinetic parameters from dynamic contrast-enhanced T₁-weighted MRI of a diffusable tracer: Standardized quantities and symbols *J. Magn. Reson. Imag.* **10** 223–232 (1999). Cited on page 59
- [119] G. Varma, R. E. Lenkinski and E. Vinogradov: Keyhole chemical exchange saturation transfer *Magn. Reson. Med.* **68** 1228–1233 (2012). Cited on pages 60 and 63
- [120] K. Oshio and D. A. Feinberg: GRASE (gradient-and spin-echo) imaging: A novel fast MRI technique *Magn. Reson. Med.* **20** 344–349 (1991). Cited on page 62
- [121] M. Viallon, Y. Berthezene, V. Callot, M. Bourgeois, H. Humblot, A. Briguët and Y. Cremillieux: Dynamic imaging of hyperpolarized ³He distribution in rat lungs using interleaved-spiral scans *NMR Biomed.* **13** 207–213 (2000). Cited on page 62
- [122] J. Du, M. Bydder, A. M. Takahashi and C. B. Chung: Two-dimensional ultrashort echo time imaging using a spiral trajectory *Magn. Reson. Imag.* **26** 304–312 (2008). Cited on page 62
- [123] D. J. Holland, C. Liu, X. Song, E. L. Mazerolle, M. T. Stevens, A. J. Sederman, L. F. Gladden, R. C. N. D’Arcy, C. V. Bowen and S. D. Beyea: Compressed sensing reconstruction improves sensitivity of variable density spiral fMRI *Magn. Reson. Med.* **70** 1634–1643 (2013). Cited on page 62
- [124] K. Block, M. Uecker and J. Frahm: Model-based iterative reconstruction for radial fast spin-echo MRI *IEEE Trans. Med. Imag.* **28** 1759–1769 (2009). Cited on page 62
- [125] D. Ma, V. Gulani, N. Seiberlich, K. Liu, J. L. Sunshine, J. L. Duerk and M. A. Griswold: Magnetic resonance fingerprinting *Nature* **495** 187–192 (2013). Cited on page 62
- [126] C. Ruckebusch and L. Blanchet: Multivariate curve resolution: A review of advanced and tailored applications and challenges *Anal. Chim. Acta* **765** 28–36 (2013). Cited on page 62
- [127] J. Jaumot, A. Juan and R. Tauler: MCR-ALS GUI 2.0: New features and applications *Chemometr. Intell. Lab.* **140** 1–12 (2015). Cited on page 62
- [128] M. El Haouaj, M. Luhmer, Y. H. Ko, K. Kim and K. Bartik: NMR study of the reversible complexation of xenon by cucurbituril *J. Chem. Soc., Perkin Trans. 2* 804–807 (2001). Cited on page 62

- [129] K. Bartik, M. Luhmer, S. J. Heyes, R. Ottinger and J. Reisse: Probing molecular cavities in α -cyclodextrin solutions by xenon NMR *J. Magn. Reson. Ser. B* **109** 164–168 (1995). Cited on page 62
- [130] T. Loftsson and M. E. Brewster: Pharmaceutical applications of cyclodextrins: basic science and product development *J. Pharm. Pharmacol.* **62** 1607–1621 (2010). Cited on page 62
- [131] C. R. Bowers, V. Storhaug, C. E. Webster, J. Bharatam, A. Cottone, R. Gianna, K. Betsey and B. J. Gaffney: Exploring surfaces and cavities in lipoxygenase and other proteins by hyperpolarized xenon-129 NMR *J. Am. Chem. Soc.* **121** 9370–9377 (1999). Cited on page 62
- [132] Z. Zu, K. Li, V. A. Janve, M. D. Does and D. F. Gochberg: Optimizing pulsed-chemical exchange saturation transfer imaging sequences *Magn. Reson. Med.* **66** 1100–1108 (2011). Cited on page 62
- [133] J.-S. Lee, P. Parasoglou, D. Xia, A. Jerschow and R. R. Regatte: Uniform magnetization transfer in chemical exchange saturation transfer magnetic resonance imaging *Sci. Rep.* **3** (2013). Cited on page 63
- [134] J. I. Friedman, M. T. McMahon, J. T. Stivers and P. C. M. Van Zijl: Indirect detection of labile solute proton spectra via the water signal using frequency-labeled exchange (FLEX) transfer *J. Am. Chem. Soc.* **132** 1813–1815 (2010). Cited on page 63
- [135] M. Doneva, H. Eggers, J. Rahmer, P. Börnert and A. Mertins: Highly undersampled 3D golden ratio radial imaging with iterative reconstruction *Proc. Intl. Soc. Mag. Reson. Med.* **16** 336 (2008). Cited on page 63
- [136] M. Schnurr, C. Witte and L. Schröder: Depolarization Laplace transform analysis of exchangeable hyperpolarized ^{129}Xe for detecting ordering phases and cholesterol content of biomembrane models *Biophys. J.* **106** 1301–1308 (2014). Cited on page 63

Abstract/Kurzzusammenfassung

Abstract

NMR detection of hyperpolarized, reversibly bound xenon using chemical exchange saturation transfer (Hyper-CEST) is a relatively new technique with great potential for the detection of dilute molecular targets, e.g. in the context of chemical sensing or molecular imaging. However, the first implementations of Hyper-CEST imaging and spectroscopy (before 2011) were still limited by relatively long acquisition times and the need for a highly consistent xenon delivery to the object (or subject) of interest. In this thesis, we present various tools to tackle these issues from a signal encoding perspective: (1) Multi-echo single-shot MRI readouts for Hyper-CEST to make efficient use of the available hyperpolarized magnetization and to accelerate the measurement process, (2) principal component analysis based data post-processing and sub-sampled data acquisition to increase the signal-to-noise ratio of spectral Hyper-CEST image series, (3) gradient encoding of the saturation frequencies to strongly accelerate *in vitro* CEST spectroscopy (ultra-fast CEST), and (4) shared magnetization after single hyperpolarization with CEST (smashCEST) to enable both Hyper-CEST imaging and spectroscopy also under conditions where the number of xenon deliveries has to be minimized due to time or signal stability restrictions. Utilizing these tools, we demonstrate new Hyper-CEST applications: For instance the monitoring of dynamic processes such as enzymatic reactions or contrast agent diffusion, and fast and sensitive spectral Hyper-CEST imaging to enable multiplexing of different contrast agents. As some of these tools have additionally been applied successfully in several other projects of our research group (e.g. the first live-cell tracking with Hyper-CEST), we are convinced that they might help to further extend the scope of molecular sensing applications using hyperpolarized xenon, eventually also in the context of future *in vivo* studies. Notably, many of the techniques presented in this thesis might also be of use for conventional CEST NMR and MRI applications using thermally polarized protons.

Kurzzusammenfassung

NMR mit hyperpolarisiertem Xenon unter Ausnutzung von Sättigungstransfer durch chemischen Austausch (Hyper-CEST) ist eine relativ neue und vielversprechende Methode zum Nachweisen von molekularen Zielstrukturen in niedrigen Konzentrationen mit Anwendungsmöglichkeiten im Bereich der Molekularbildgebung oder der (bio-)chemischen Probenanalyse.

In ersten Studien (vor 2011) war die praktische Anwendbarkeit von Hyper-CEST zur Bildgebung und Spektroskopie jedoch noch durch relativ lange Aufnahmezeiten und die Notwendigkeit einer sehr stabilen Xenon-Anlieferung beschränkt. In der vorliegenden Arbeit werden mehrere Methoden aus den Bereichen der Bild- und Signalverarbeitung und -kodierung vorgestellt, um diese Einschränkungen zu reduzieren: (1) Multi-echo single-shot MRI-Techniken für Hyper-CEST um die vorhandene, hyperpolarisierte Magnetisierung optimal zu nutzen und um die Aufnahmedauer zu verkürzen, (2) auf Hauptkomponentenanalyse basierende Bildverarbeitung sowie Unterabtastung bei der Bildaufnahme um das Signal-Rausch-Verhältnis von spektralen Hyper-CEST Bildserien zu erhöhen, (3) Gradientenkodierung der Sättigungsfrequenzen um die *in vitro* CEST Spektroskopie stark zu beschleunigen (ultrafast CEST), und (4) smashCEST (shared magnetization after single hyperpolarization – also „geteilte Magnetisierung nach einer einzigen Hyperpolarisierung“ – für CEST) um Hyper-CEST Spektroskopie und Bildgebung auch dann zu ermöglichen, wenn die Anzahl an Xenon-Anlieferungen aus Zeit- oder Stabilitätsgründen minimiert werden muss. Diese Methoden eröffnen neue Anwendungsmöglichkeiten für Hyper-CEST, z.B. die Beobachtung von dynamischen Prozessen wie etwa enzymatischen Reaktionen oder der Diffusion von Kontrastmittelmolekülen mit hoher zeitlicher Auflösung, oder auch die schnelle Aufnahme spektraler Bildserien, um gleichzeitig mehrere verschiedene Kontrastmittel nachzuweisen („Multiplexing“). Einige dieser Techniken wurden weiterhin erfolgreich in mehreren anderen Projekten unserer Arbeitsgruppe eingesetzt, wie beispielsweise zum erstmaligen Nachverfolgen von lebendigen Zellen („live cell tracking“) mittels Hyper-CEST Bildgebung. Sie könnten daher auch in Zukunft dazu beitragen, die Anwendbarkeit von NMR mit hyperpolarisiertem Xenon weiter auszuweiten, insbesondere im Hinblick auf kommende *in vivo* Studien. Es ist außerdem darauf hinzuweisen, dass viele der hier vorgestellten Methoden auch in konventionellen CEST-MR-Anwendungen mit thermisch polarisierten Protonen von Nutzen sein könnten.



Acknowledgments

For reasons of data protection, the acknowledgments are not included in the online version.



Curriculum Vitae

For reasons of data protection, the curriculum vitae is not included in the online version.



Attached publications

The publications attached to the print version of this document are not available in the online version due to copyright reasons.

